



Substrate Entrainment, Depositional Relief, and Sediment Capture: Impact of a Submarine Landslide on Flow Process and Sediment Supply

A. Martínez-Doñate^{1*}, A. M-L. J. Privat², D. M. Hodgson², C. A-L. Jackson¹, I. A. Kane¹, Y. T. Spychala³, R. A. Duller⁴, C. Stevenson⁴, E. Keavney², E. Schwarz⁵ and S. S. Flint¹

¹School of Earth and Environmental Sciences, University of Manchester, Manchester, United Kingdom, ²School of Earth and Environment, University of Leeds, Leeds, United Kingdom, ³Institute for Geology, Leibniz University Hannover, Hannover, Germany, ⁴Department on Earth, Ocean, and Ecological Sciences, University of Liverpool, Liverpool, United Kingdom, ⁵Centro de Investigaciones Geológicas (CIG), La Plata, Argentina

OPEN ACCESS

Edited by:

Fabiano Gamberi,
Institute of Marine Science (CNR), Italy

Reviewed by:

Kei Ogata,
University of Naples Federico II, Italy
Victoria Valdez Buso,
Federal University of Paraná, Brazil
Mattia Marini,
University of Milan, Italy

*Correspondence:

A. Martínez-Doñate
ander.martinez-donate@
manchester.ac.uk

Specialty section:

This article was submitted to
Sedimentology, Stratigraphy and
Diagenesis,
a section of the journal
Frontiers in Earth Science

Received: 12 August 2021

Accepted: 27 October 2021

Published: 16 November 2021

Citation:

Martínez-Doñate A, Privat AM-LJ, Hodgson DM, Jackson CA-L, Kane IA, Spychala YT, Duller RA, Stevenson C, Keavney E, Schwarz E and Flint SS (2021) Substrate Entrainment, Depositional Relief, and Sediment Capture: Impact of a Submarine Landslide on Flow Process and Sediment Supply. *Front. Earth Sci.* 9:757617. doi: 10.3389/feart.2021.757617

Submarine landslides can generate complicated patterns of seafloor relief that influence subsequent flow behaviour and sediment dispersal patterns. In subsurface studies, the term mass transport deposits (MTDs) is commonly used and covers a range of processes and resultant deposits. While the large-scale morphology of submarine landslide deposits can be resolved in seismic reflection data, the nature of their upper surface and its impact on both facies distributions and stratal architecture of overlying deposits is rarely resolvable. However, field-based studies often allow a more detailed characterisation of the deposit. The early post-rift Middle Jurassic deep-water succession of the Los Molles Formation is exceptionally well-exposed along a dip-orientated WSW-ENE outcrop belt in the Chacay Melehue depocentre, Neuquén Basin, Argentina. We correlate 27 sedimentary logs constrained by marker beds to document the sedimentology and architecture of a >47 m thick and at least 9.6 km long debrite, which contains two different types of megaclasts. The debrite overlies ramps and steps, indicating erosion and substrate entrainment. Two distinct sandstone-dominated units overlie the debrite. The lower sandstone unit is characterised by: 1) abrupt thickness changes, wedging and progressive rotation of laminae in sandstone beds associated with growth strata; and 2) detached sandstone load balls within the underlying debrite. The combination of these features suggests syn-sedimentary foundering processes due to density instabilities at the top of the fluid-saturated mud-rich debrite. The debrite relief controlled the spatial distribution of foundered sandstones. The upper sandstone unit is characterised by thin-bedded deposits, locally overlain by medium-to thick-bedded lobe axis/off-axis deposits. The thin-beds show local thinning and onlapping onto the debrite, where it develops its highest relief. Facies distributions and stacking patterns record the progradation of submarine lobes and their complex interaction with long-lived debrite-related topography. The emplacement of a kilometre-scale debrite in an otherwise mud-rich basinal setting and accumulation of overlying sand-rich deposits suggests a genetic link between the mass-wasting event and transient coarse clastic sediment supply to an otherwise sand-starved part of the basin. Therefore, submarine landslides demonstrably

impact the routing and behaviour of subsequent sediment gravity flows, which must be considered when predicting facies distributions and palaeoenvironments above MTDs in subsurface datasets.

Keywords: foundering, dynamic topography, confinement, submarine landslide deposits, submarine lobe, Neuquén basin (Argentina)

INTRODUCTION

Submarine landslide deposits, olistostromes (Flores, 1955), or Mass Transport Deposits (MTDs) (Nardin et al., 1979), are sedimentary bodies that have been translated downslope from high to low gradient slopes as a result of mass failure and gravitational processes (Hampton et al., 1995; Moscardelli and Wood, 2008; Ogata et al., 2012; Festa et al., 2016; Kneller et al., 2016). The typically cohesive nature of the flows enables the transportation of large clasts (>4.1m diameter; herein named megaclasts, *sensu* Blair and McPherson, 1999) (Labaume et al., 1987; Payros et al., 1999; McGilvery and Cook, 2003; Lee et al., 2004; Jackson, 2011; Ogata et al., 2012; Hodgson et al., 2019; Nwoko et al., 2020a). Megaclasts within MTDs are sourced either from headwall areas or entrained from the substrate (Festa et al., 2016; Ogata et al., 2019). These features, accompanied by syn- and post-depositional faulting (Dykstra, 2005; Dykstra et al., 2011), generate the topographically irregular upper surfaces of MTDs (Moscardelli et al., 2006; Bull et al., 2009).

Deep-water sediment gravity flows interact with the rugose topography of MTDs, which influences flow behaviour, deceleration and steadiness (Lowe and Guy, 2000; Armitage et al., 2009; Jackson and Johnson, 2009; Fairweather, 2014; Ortiz-Karpf et al., 2015, 2017; Steventon et al., 2021), and therefore dispersal patterns and depositional architecture (Kneller et al., 2016). MTD surface relief has been shown to affect facies distribution and associated sedimentary architecture; this has been reported from both outcrop (Pickering and Corregidor, 2005; Armitage et al., 2009; Dykstra et al., 2011; Fallgatter et al., 2017; Brooks et al., 2018; Valdez et al., 2019) and subsurface studies (Ortiz-Karpf et al., 2017; Nwoko et al., 2020b). However, MTDs may continue to deform after initial emplacement through creeping processes (e.g. Butler and McCaffrey, 2010) or secondary mass movements (Sobiesiak et al., 2016). Furthermore, the high water content within newly deposited MTDs promotes active dewatering at their upper surface (Mulder and Alexander, 2001; Talling et al., 2012; Browne et al., 2020) associated with local instabilities and movement (Iverson, 1997; Major and Iverson, 1999; Van der Merwe et al., 2009). Fluids can also generate overpressure along with the interface between MTDs and its sediment cover, exploiting pathways created by internal MTD deformation (Ogata et al., 2012; Migeon et al., 2014). Therefore, the interaction between the initial topographic relief of MTDs, dewatering processes, post-depositional deformation and subsequent sediment gravity flows (and their deposits) is highly dynamic and inherently complex (e.g. Alves, 2015). A better understanding of sedimentary processes above MTDs can help subsurface predictions of facies distributions, which might

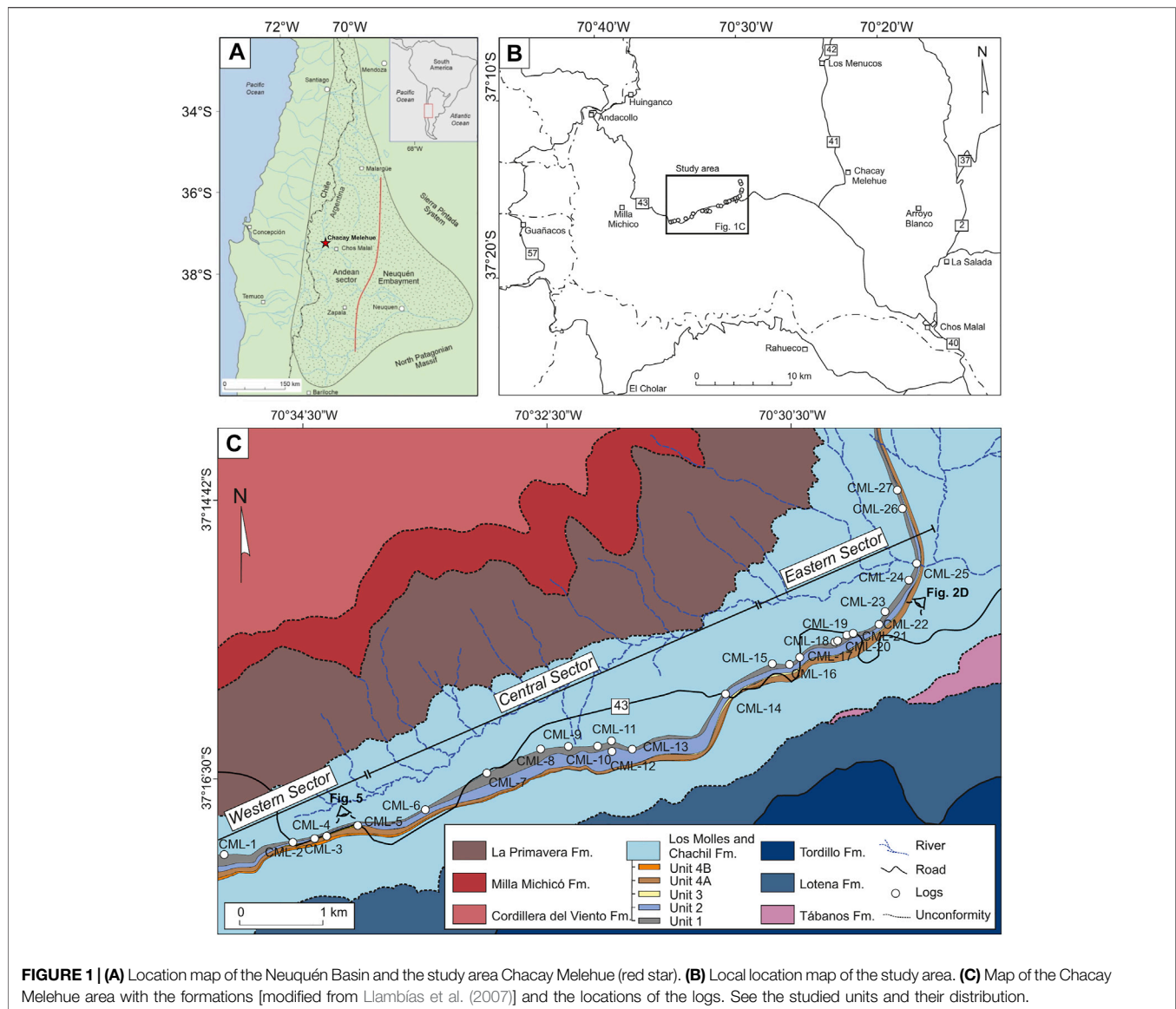
have been overlooked due to variable seismic resolution and core coverage. Therefore, detailed field-based studies can help to bridge the resolution gap.

Here, we aim to understand an exceptionally well-exposed debrite and overlying sand-rich strata in the Bathonian Los Molles Formation, which were physically correlated over 9.6 km along a depositional dip transect in the Chacay Melehue depocenter (Neuquén Basin, Argentina). The objectives of this study are to 1) document the anatomy and stratigraphic architecture of the debrite, 2) investigate the impact of the dynamic upper relief on the overlying heterolithic and sand-rich strata, and 3) discuss the role that mass-wasting processes may have played as a trigger for subsequent sand-rich sediment supply.

GEOLOGICAL SETTING

The Neuquén Basin is located in central-western Argentina and central-eastern Chile, covering an area of 160,000 km² (Figure 1A). The basin is bounded to the north-east by the Sierra Pintada, to the south by the North Patagonian Massif, and since the Early Jurassic, by the early Andean magmatic arc to the west (Legarreta and Gulisano, 1989; Suárez and de la Cruz, 1997; Franzese and Spalletti, 2001; Howell et al., 2005). The Neuquén Basin contains a >6 km-thick sedimentary succession that spans the Mesozoic to the Late Cenozoic and records several unconformities related to tectonic phases (Vergani et al., 1995; Legarreta and Uliana, 1996; Howell et al., 2005). Three key tectonic phases are recognised (Vergani et al., 1995; Franzese and Spalletti, 2001; Franzese et al., 2003): 1) Triassic-to-Early Jurassic rifting and the onset of subsidence; 2) Early Jurassic-to-Early Cretaceous post-rift thermal subsidence associated with the development of the Andean magmatic arc and back-arc basin; and 3) Late Cretaceous-to-Early Cenozoic Andean compression and foreland basin development. In the western sector of the Central Neuquén Basin, the deep- to shallow-marine deposits of the early post-rift Cuyo Group (Lower-to-Middle Jurassic) (Gulisano et al., 1984) unconformably overlie the continental syn-rift volcano-sedimentary deposits of the Precuyano Group (Gulisano et al., 1984; Gulisano and Gutiérrez Pleimling, 1995; Legarreta and Uliana, 1996; Pángaro et al., 2009; Leanza et al., 2013) or the Palaeozoic basement of the Choiyoi Group (Llambías et al., 2003, 2007) (Figure 2A).

Our investigation focuses on the Early Bathonian stratigraphy of the Upper Los Molles Formation, which forms a ~70 m thick interval characterised by ammonite-rich black shales and heterolithic successions comprising tuff layers with an intervening MTD and sandstone deposits (Figure 1B).



Study Area—Chacay Melehue Depocentre

The succession in the Chacay Melehue area was deposited in a half-graben (~20 km long) (Manceda and Figueroa, 1995; Llambías et al., 2007; Leanza et al., 2013) that occupied the western and deepest part of a broader early post-rift depocentre in the Central Neuquén Basin (~65 km long) (Manceda and Figueroa, 1995; Veiga et al., 2013). The half-graben shows a strong asymmetry due to a steep western margin characterised by the development of the early Andean magmatic arc and location of a major syn-rift fault (Manceda and Figueroa, 1995; Suárez and de la Cruz, 1997; Vicente, 2005), which contrasts with the stable and gently dipping eastern cratonic margin (Spalletti et al., 2012; Veiga et al., 2013). Deposition of the Los Molles Formation took place during a period of thermal subsidence and regional marine transgression across complex inherited rift topography, which promoted the reduction of sediment supply and sand starvation in this part of

the basin (Spalletti et al., 2012; Veiga et al., 2013). The proximity to the volcanic arc (~30 km to the west), the abundant volcanoclastic deposits (Zöllner and Amos, 1973; Rosenfeld and Volldaeimer, 1980; Gulisano and Gutiérrez Pleimling, 1995; Suárez and de la Cruz, 1997; Vicente, 2005; Llambías et al., 2007), and palaeocurrent measurements in sandstones indicating a general southeastwards trend reveals that sediment supply feeding the Chacay Melehue area during the post-rift was sourced from the western magmatic arc (Gulisano et al., 1984; Vicente, 2005). The deep-marine deposits of Los Molles Formation (Weaver, 1931) overlie shallow-marine tuffaceous clastic deposits (De La Cruz and Suarez, 1997; Llambías and Leanza, 2005) and carbonate deposits of the Chachil Formation (Pliensbachian to Early Weaver, 1942; Kamo and Riccardi, 2009; Leanza et al., 2013; Riccardi and Kamo, 2014), deposited with the first marine incursion in the basin (Gulisano and Gutiérrez Pleimling, 1995; Leanza et al.,

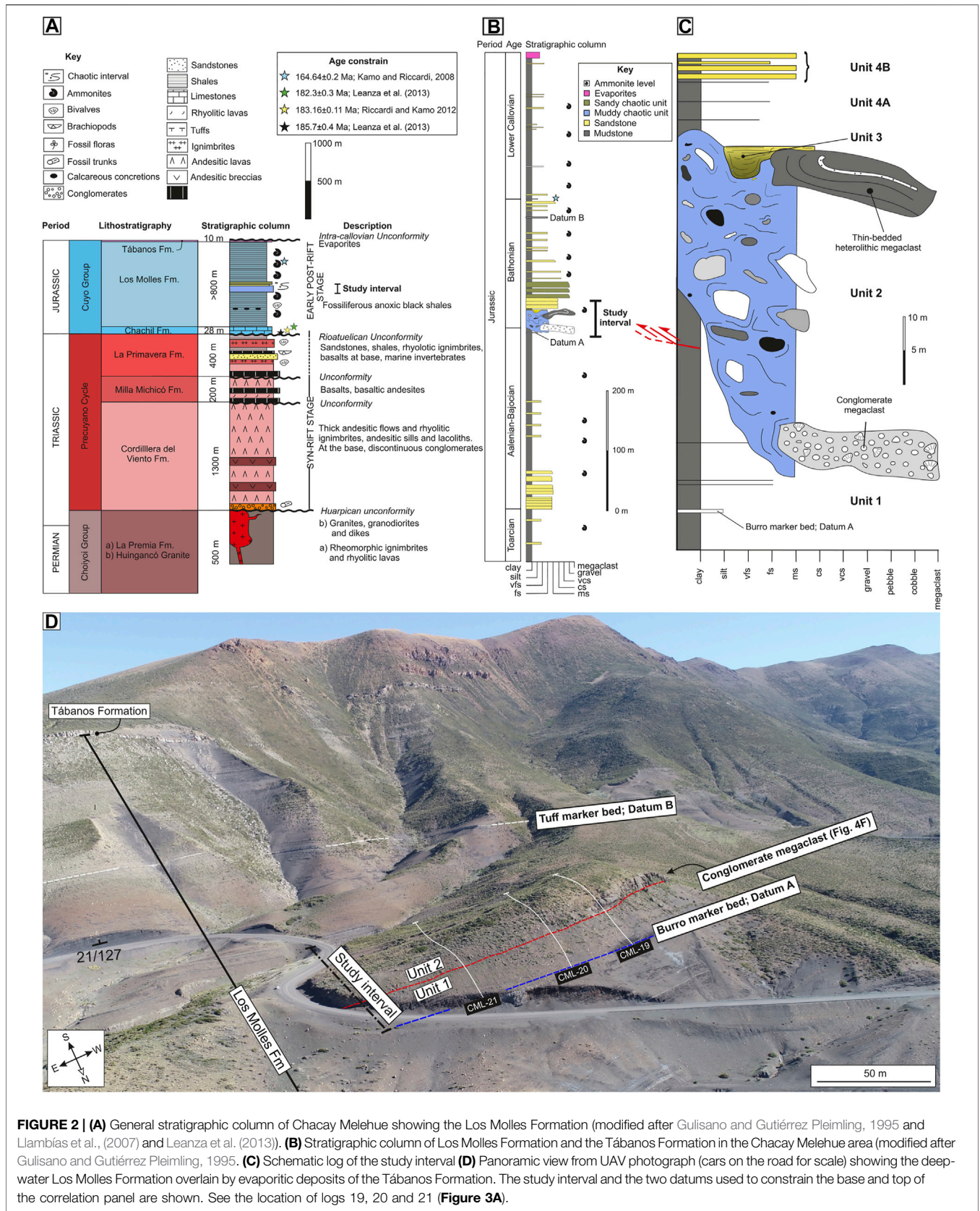


FIGURE 2 | (A) General stratigraphic column of Chacay Melehue showing the Los Molles Formation (modified after Gulisano and Gutiérrez Pleimling, 1995 and Llamás et al., (2007) and Leanza et al. (2013)). **(B)** Stratigraphic column of Los Molles Formation and the Tábanos Formation in the Chacay Melehue area (modified after Gulisano and Gutiérrez Pleimling, 1995). **(C)** Schematic log of the study interval **(D)** Panoramic view from UAV photograph (cars on the road for scale) showing the deep-water Los Molles Formation overlain by evaporitic deposits of the Tábanos Formation. The study interval and the two datums used to constrain the base and top of the correlation panel are shown. See the location of logs 19, 20 and 21 (Figure 3A).

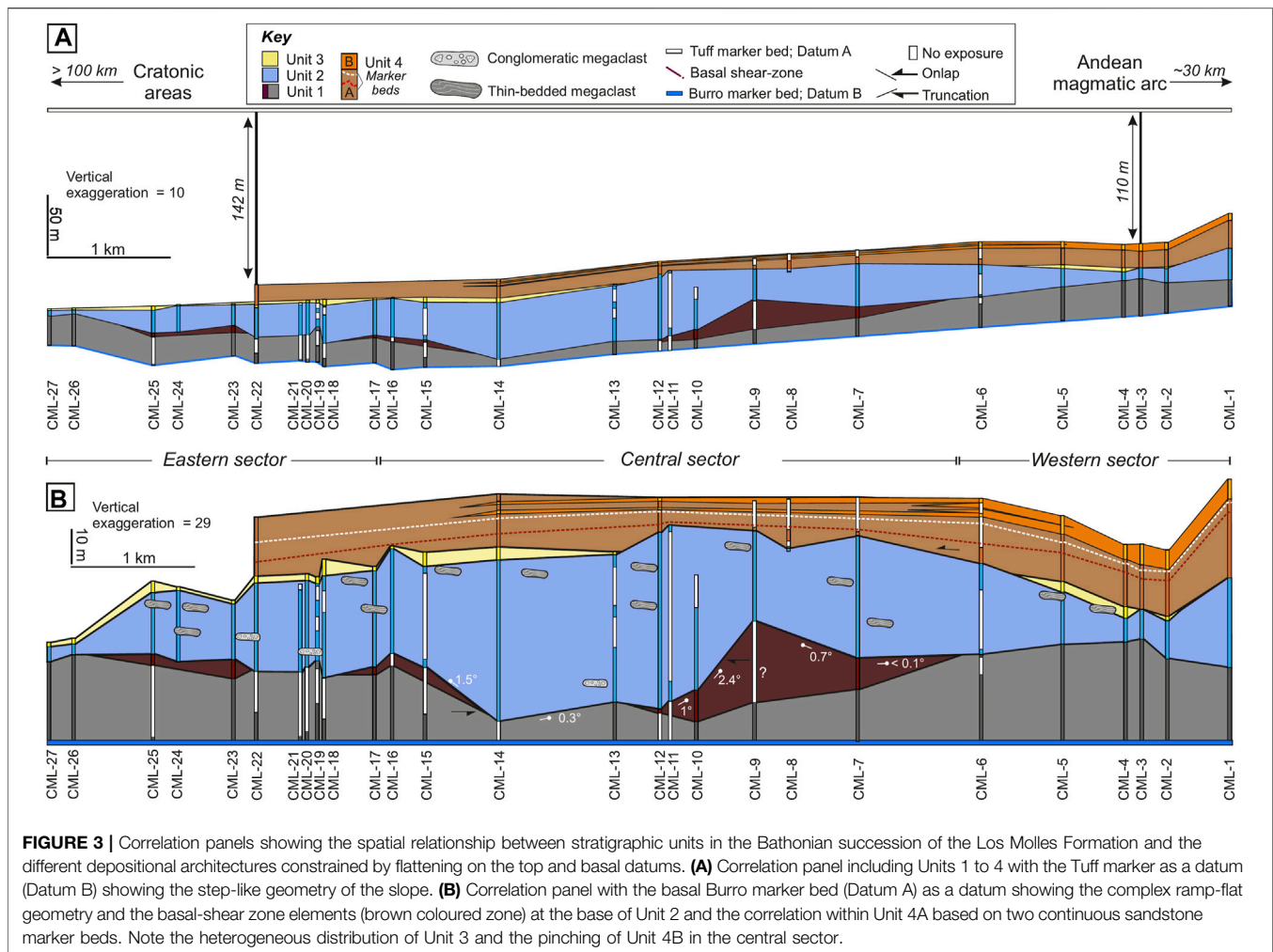


FIGURE 3 | Correlation panels showing the spatial relationship between stratigraphic units in the Bathonian succession of the Los Molles Formation and the different depositional architectures constrained by flattening on the top and basal datums. **(A)** Correlation panel including Units 1 to 4 with the Tuff marker as a datum (Datum B) showing the step-like geometry of the slope. **(B)** Correlation panel with the basal Burro marker bed (Datum A) as a datum showing the complex ramp-flat geometry and the basal-shear zone elements (brown coloured zone) at the base of Unit 2 and the correlation within Unit 4A based on two continuous sandstone marker beds. Note the heterogeneous distribution of Unit 3 and the pinching of Unit 4B in the central sector.

2013) (**Figure 2A**). Chronostratigraphic studies based on ammonite biostratigraphy (Gulisano and Gutiérrez Pleimling, 1995; Riccardi, 2008) and U-Pb radiometric dating (Kamo and Riccardi, 2009; Leanza et al., 2013; Riccardi and Kamo, 2014), place the Los Molles Formation in the Chacay Melehue region as Early Toarcian-to-Early Callovian in age (Gulisano and Gutiérrez Pleimling, 1995) (**Figure 2C**). The succession of the Los Molles Formation in the Chacay Melehue depocentre is 850 m thick (**Figure 2B**). A 55 m thick sandstone-prone interval in the lower succession represents an Aalenian turbidite system (interval II of Gulisano and Gutiérrez Pleimling, 1995). The overlying Bathonian section of the Los Molles Formation (up to 200 m thick) (**Figure 2B**) is mainly represented by mudstone and heterolithic successions, including a 70 m thick interval (study interval; **Figure 2C**) of deformed sand- and mud-rich deposits (interval IV of Gulisano and Gutiérrez Pleimling, 1995). The overlying Lower Callovian strata of the Los Molles Formation is characterised by a 300 m thick interval of thin-bedded mudstone. It is overlain by either the fluvial Lotena Formation (Gulisano and Gutiérrez Pleimling, 1995; Veiga et al., 2011) or evaporites (Tábanos Formation; **Figure 2D**), which record a period of

basin desiccation (Legarreta, 1991; Gulisano and Gutiérrez Pleimling, 1995; Legarreta and Uliana, 1996).

METHODOLOGY

The sedimentology and stratigraphic architecture of a 70 m thick interval (**Figures 2C, 3**) within the Upper Los Molles Formation were investigated along a 9.6 km long and WSW-ENE orientated outcrop belt (**Figures 1B,C**). The succession dips 10–20° to the SE, with minimal structural overprint from the later tectonic inversion. Twenty-seven (27) sedimentary logs were measured at 1:25 to 1:40 scale along this transect (CML-0 to CML-27 from SW to NE) to document the broad depositional architecture of 4 different units (Unit 1, 2, 3, 4A and B) (**Figure 1C**). Ten detailed logs were measured at a 1:2 scale at specific locations to document fine-scale thickness and facies changes. Four marker beds were used to build a robust physical correlation between sedimentary logs (**Figures 2, 3**). The marker beds are 1) Datum A, or the “Burro” marker bed, a light-grey indurated graded siltstone at the base of the study interval (**Figures 2A, 3, 4A**); 2) a gravelly thin-

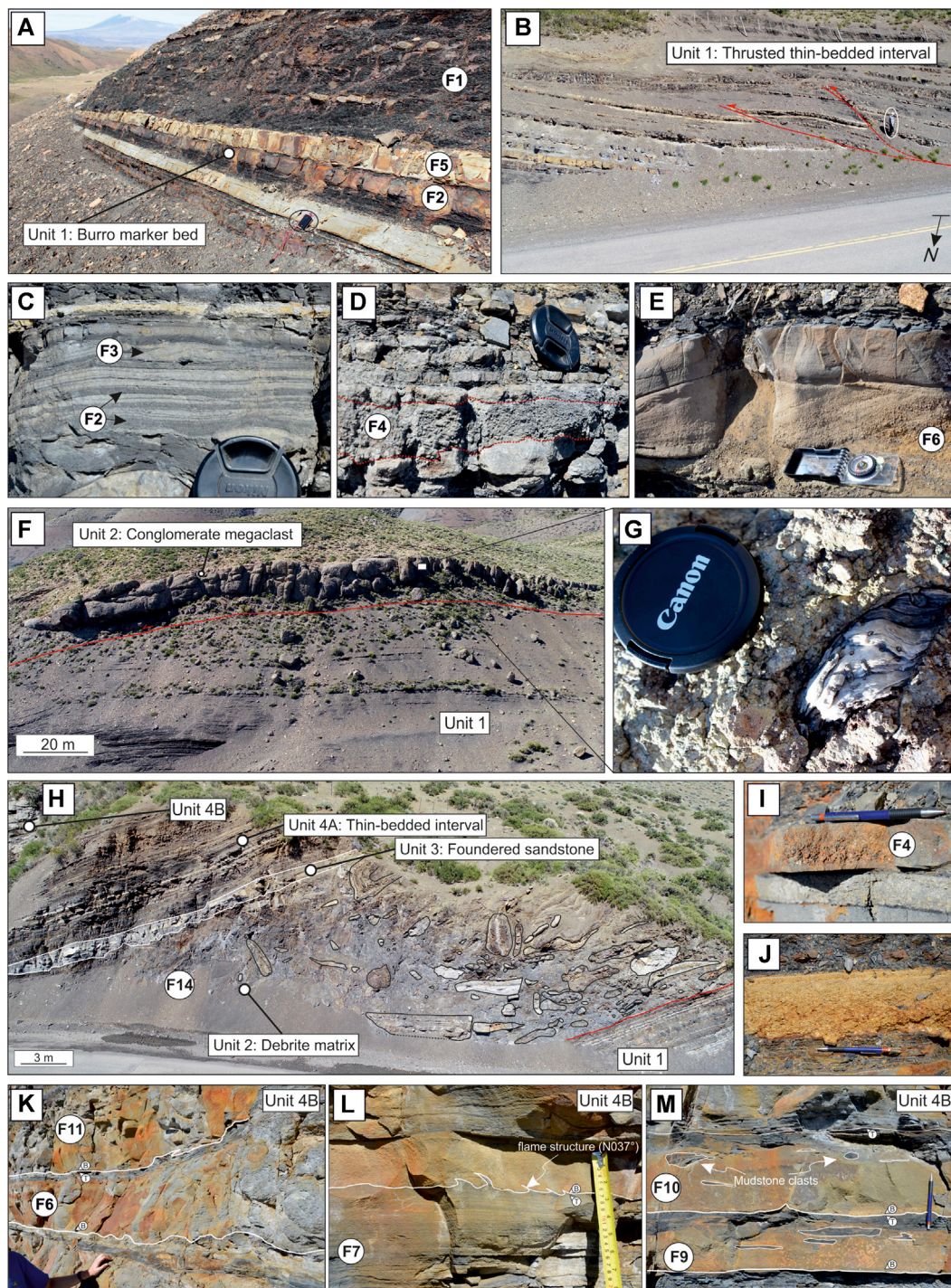


FIGURE 4 | Representative sedimentary facies photos. **(A)** Unit 1: Planar-laminated mudstone (F1) with a few thin- to medium-bedded intercalated siltstone beds (F2) (Burro marker bed; Datum A) and sandstone beds (F5). **(B)** Unit 1: Basal shear-zone characterised by imbricated thrusts with drag folding. **(C)** Unit 4A: Heterolithic deposits consisting in the alternation between siltstones (F2) to (very) fine-grained sandstones (F3). **(D)** Unit 4A: Gravelly thin bed (F4) locally eroded into fine-grained sandstones (F3). **(E)** Unit 4A: Medium-bedded sandstones with cross-bedding (F6). **(F)** Unit 2: 140 m long conglomerate megaclast, bearing oyster and belemnite fragments, and sitting above Unit 1. Oyster fragment highlighted in the inset box **(G)**. **(H)** Unit 2, 3 and 4A: Foundered sandstones onlapping the matrix-rich debrite (F14) with deformed heterolithic megaclasts draped by the thin-bedded deposits of Unit 4A. **(I)** Unit 4A: Gravelly and **(J)** Tuff-marker bed within 4A. See the correlation **Panels 3B, 8** (red and white dashed lines). **(K)** Unit 4B: Amalgamated medium- (F6) to thick-bedded (F11) sandstones. **(L)** Unit 4B: Medium-bedded banded sandstone (F7) overlain by massive matrix-poor sandstones (F5). Note the vergent flame structures within the amalgamation surface **(M)** Unit 4B: Thin- (F9) and medium-bedded (F10) hybrid event beds type 2 (cf. Houghton et al., 2009) with a linked debrite consisting of matrix-rich sandy division with elongated mudstone clasts.

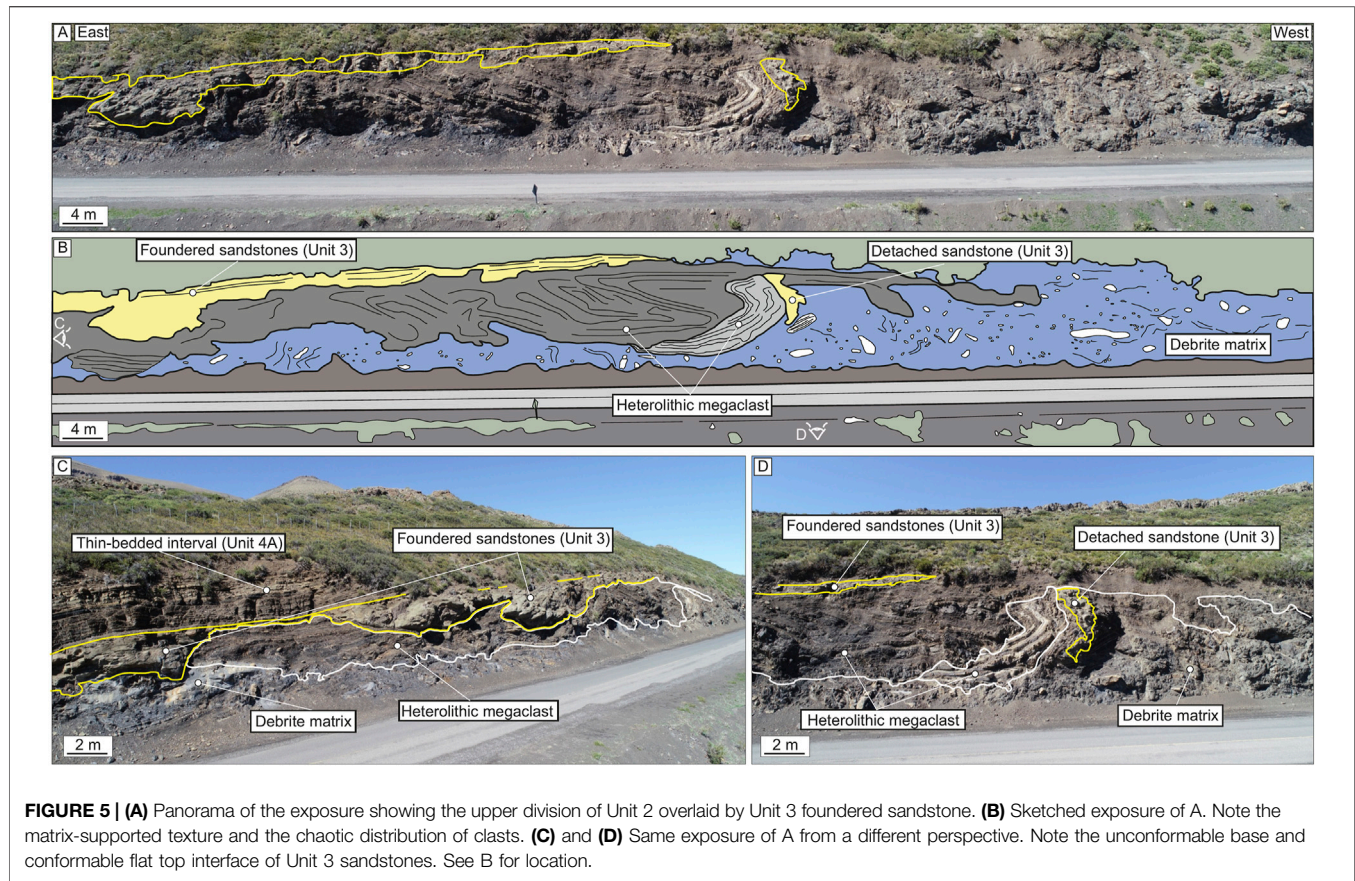


FIGURE 5 | (A) Panorama of the exposure showing the upper division of Unit 2 overlaid by Unit 3 foundered sandstone. (B) Sketched exposure of A. Note the matrix-supported texture and the chaotic distribution of clasts. (C) and (D) Same exposure of A from a different perspective. Note the unconformable base and conformable flat top interface of Unit 3 sandstones. See B for location.

bed (Figure 4F) and 3) a tuff layer (Figure 4G), both within one of the studied units (Unit 4A); and 4) Datum B, a tuff layer overlying the study interval (100–150 m above) across the study area (Figures 2D, 3). Uncrewed Aerial Vehicle (UAV) photogrammetry (Figures 2D, 5) was used in conjunction with standard field techniques, such as mapping and logging, to capture the micro- and macro-scale features of the investigated stratigraphic units. Fifty-eight (58) palaeocurrent measurements were collected from ripples, cross-bedding, flame structure and convolute lamination vergence from bed tops of sandstones, and plotted in rose diagrams.

RESULTS: SUBDIVISION AND CHARACTERISATION OF SEDIMENTARY UNITS 1–4

The study interval is subdivided informally into four different units (Figure 2C), based on their distinctive facies (Table 1) and stratal relationships.

Unit 1

Description: Unit 1 is 5.5–28 m thick and contains the Burro marker bed (Datum A) (Figure 2C), a light-grey indurated graded siltstone that is sharply overlain by light-grey fine-grained, planar-parallel laminated sandstone (Figure 4A). This

unit is truncated by the basal surface of Unit 2 and is thinnest in the central sector of the exposure (see sections CML-9 to CML-16 Figure 3). Unit 1 comprises a heterolithic succession of planar-parallel laminated mudstones (F1) and thin-bedded (<0.1 m thick) normally-graded, well-sorted sandstones (F2) to very fine-grained sandstones (F3), and occasional medium-bedded structureless sandstones (F5) (Figures 4A,C). When traced from west to east, the thin-bedded sandstones show subtle lateral fining and thinning, transitioning from heterolithic succession to mudstone-prone succession. Unit 1 is rich in ammonites, belemnite rostrums and bivalves, as well as calcareous concretions (Damborenea, 1990; Gulisano and Gutiérrez Pleimling, 1995; Riccardi et al., 2011).

The central and eastern sectors contain a discrete stratigraphic interval that exhibits deformed bedding (Figure 4B). This interval is thickest (at least 10 m; Figure 3) in the central sector, where, internally, it exhibits an array of imbricated decametre-scale east-verging thrusts (offset <2 m) and associated drag folds. The thrusts originate from a bed parallel surface, leaving the underlying bedding undeformed (Figure 4B). In the eastern sector, a thin (~5 m thick) interval of intense deformation is characterised by open folds and minor thrusts (offset <1 m) (Figure 4B). Unit 1 stratigraphy in the western sector lacks any deformation.

Interpretation: The laminated mudstones, graded siltstones and thin sandstone beds are interpreted as deposits of low-density

TABLE 1 | Descriptions of the facies recognised in the Los Molles stratigraphy of the Chacay Melehue area, including lithologies, thicknesses, and interpretations of their depositional processes.

Lithofacies	Lithology	Description	Thickness	Process interpretation
F1: Laminated mudstone	Mudstone	Dark-coloured planar parallel laminated mudstone with Ammonites. Concretionary horizons are common	0.1–3 cm	Deposits from very dilute sediment gravity under relative dysoxic-anoxic conditions (Trabucho-Alexandre et al., 2012; Könitzer et al., 2014)
F2: Graded siltstone	Graded siltstone	Normally-graded from silty bases to mud-rich tops. Usually structureless, although planar parallel-laminations are common	1–5 cm	Deposition under low-density turbidity current (Allen, 1971)
F3: Thin-bedded fine-grained sandstones	Very fine- to fine-grained sandstones	Normally-graded, well-sorted thin-beds. Fine-grained bases and very fine-grained tops. Structureless at the base with planar laminated tops. Rare starved ripple lamination at bed tops	1–10 cm	Deposition and tractional reworking by low-density turbidity current (Allen, 1971, 1982; Jobe et al., 2012)
F4: Thin-bedded granular sandstones	Granular- to medium-grained sandstones	Normally-graded, very well-sorted, coarse-grained to granular-sandstones. Sharp planar base and top	1–10 cm	Deposition from turbidity currents
F5: Medium-bedded sandstones	Very fine- to medium-grained sandstone	Structureless, normally-graded sandstones. Bed bases are medium-grained, grading up until fine-grained	10–50 cm	Deposition from medium-density turbidity currents. High-aggradation rates inhibited the formation of sedimentary structures (Talling et al., 2012)
F6: Thin-bedded cross-stratified sandstones	Granular- to medium-grained sandstones	Normally-graded, well-sorted thin-beds. Foreset heights range from 5 to 7 cm, and angles vary between 10° and 35°. Erosional bases are common—sharp contacts, with planar base and undulatory top	5–10 cm	Deposition and tractional reworking by turbidity currents (Tinterri, 2011)
F7: Medium-bedded banded sandstones	Banded sandstones with sharp alternation between darker and lighter bands. Lighter bands are grain-supported, while darker bands are matrix-supported and lack mudstone clasts	Sandstones comprising alternation between matrix-poor light bands and matrix-rich dark bands (0.2–2 cm thick). Similar grain size (fine to medium) along with different bands. Heterolithic bedforms and pinch-and-swell geometries can be developed. The bed bases can be structureless	10–50 cm	Deposits beneath mud-rich transitional plug flow formed by tractional reworking within the upper stage plane bed flow regime (Baas et al., 2009, 2011, 2016; Stevenson et al., 2020)
F8: Thick-bedded banded sandstones with mudstone clast	Banded sandstones with diffuse alternation between darker and lighter bands. Lighter bands are grain-supported, while darker bands are matrix-supported, with abundant mudstone clasts	Sandstones comprising banding between matrix-poor light bands and matrix-rich mudstone clast (millimetric scale) bearing dark bands (0.5–2 cm). Banding is diffuse and can be developed throughout the bed or from the middle to the top parts of a bed, commonly overlaid by convolute lamination. Laminae show local tilting and increasing spacing between laminae	50–150 cm	Rapid aggradation and episodic damping of near bed turbulence due to clay flocs disaggregation (Lowe and Guy, 2000). Increasing spacing between laminae is attributed to growth strata due to foundering processes
F9: Thin-bedded hybrid event beds	Silty sandstone	Matrix poor bases with linked argillaceous, ungraded and poorly-sorted top divisions	1–10 cm	Distal deposits are the product of en masse deposition and potentially behaving as transitional to laminar flows (Kane et al., 2017)
F10: Medium-bedded hybrid event beds	Bipartite sandstones with matrix-poor basal divisions and upper argillaceous mudstone-clast prone division	Bipartite sandstone beds are characterised by a matrix-poor structureless lower division passing gradually into linked mudstone clasts matrix-rich upper division	10–50 cm	Deposits formed under transitional flows. Erosion and incorporation of intrabasinal clasts. The entrained substrate was rapidly disaggregated within the flow resulting in clast-rich and clay-rich divisions at the bed top. The flows increased in concentration but had not developed stable density stratification (Haughton et al., 2003; Davis et al., 2009; Hodgson, 2009; Kane and Pontén, 2012; Kane et al., 2017)
F11: thick-bedded sandstones	Structureless sandstone	Structureless, thick-bedded argillaceous sandstones, lacking mudstone clasts. High amalgamation	0.5–1.2 m	Deposition under high-density turbidity currents (sensu Lowe, 1982), formed by incremental layer-by-layer deposition with

(Continued on following page)

TABLE 1 | (Continued) Descriptions of the facies recognised in the Los Molles stratigraphy of the Chacay Melehue area, including lithologies, thicknesses, and interpretations of their depositional processes.

Lithofacies	Lithology	Description	Thickness	Process interpretation
		rations and erosional beds when lying above fine-grained intervals. Banding is locally developed at bed tops, alternating between matrix-poor light bands and matrix-rich dark bands (0.2–2 cm thick). Similar grain size (fine to medium) along with different bands. Heterolithic bedforms and pinch-and-swell geometries can be developed		high aggradation rates (Kneller and Branney, 1995; Sumner et al., 2008; Talling et al., 2012). The banding represents planar lamination (Bouma Tb division) (Stevenson et al., 2020)
F12: Thick-bedded structureless matrix-poor sandstones with normally-graded mudstone clast	Structureless sandstones with a mudstone clast at the base	Structureless thick-bedded, medium- to coarse-grained, crudely normally-graded sandstones, with low-matrix content. They contain some mudstone clasts (0.1–1 m) with diffuse boundaries preferentially located at the base, which show coarse tail grading. Mudstone diapirs along the basal interface are common	0.5–2 m	Deposition under high-density turbidity currents (sensu Lowe, 1982), formed by incremental layer-by-layer deposition with very high aggradation rates (Kneller and Branney, 1995; Sumner et al., 2008; Talling et al., 2012). Mudstone clast is entrained due to erosion of an unconsolidated debrite (Unit 2) and syn-sedimentary buoyancy product of density instabilities (Owen, 1987, 2003)
F13: Thick-bedded structureless matrix-rich sandstones with ungraded mudstone clast	Argillaceous sandstone with abundant mudstone clasts	Structureless thick-bedded, fine- to medium-grained, ungraded sandstones with very high matrix content and abundant decimetric mudstone clasts (0.1–1 m) randomly distributed	0.5–2 m	Moderate-strength cohesive debris flows derived from mudstone clast entrainment and disaggregation. Mudstone clasts are supported by their positive buoyancy with respect to the surrounding matrix and the matrix strength (Talling et al., 2012)
F14: matrix-supported conglomerates	Mud-rich medium-grained sandstone to sandy mudstone	Poorly sorted, ungraded with a chaotic distribution of outsized clasts (up to 140 m long). Irregular and sharp contacts. Bases can be erosive and undulatory tops	7.4–47.9 m	Cohesive debris-flow deposits (sensu Talling et al., 2012). with near-instantaneous deposition from a flow with high yield strength and buoyant support

turbidity currents (Allen, 1982; Trabuco-Alexandre et al., 2012; Könitzer et al., 2014), whereas the medium-bedded sandstones represent the deposits of medium- to high-density turbidity current (Talling et al., 2012). The laterally extensive character, mudstone dominance, and overall eastward (down-dip) fining and thinning trend of thin-bedded sandstones of Unit 1 suggest deposition from low-energy sediment gravity flows in distal areas (e.g., Mutti, 1977), with possible distal lobe fringe deposits (Boulestex et al., 2020). The discrete intervals of deformed bedding found in the upper parts of Unit 1 represent a post-depositional sheared zone linked to the overlying Unit 2.

Unit 2

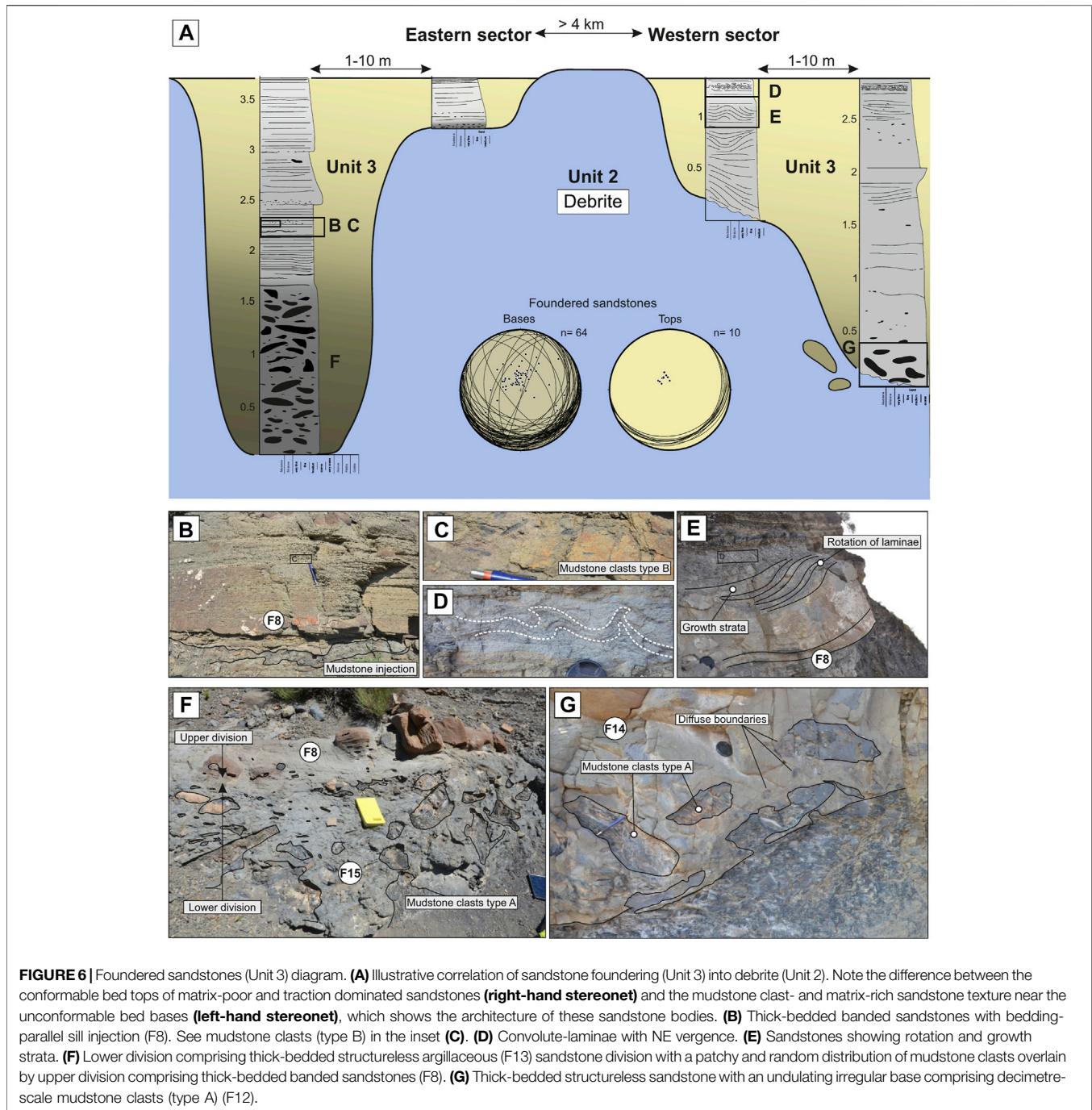
Description: Unit 2 has an unconformable basal contact that truncates Unit 1 in the central sector (Figure 3). The relief of the basal contact is characterised by down- and up-stepping segments (ramps, >2°) linked by bedding-parallel segments (flats). The average thickness of Unit 2 is 20–30 m but can locally reach >47 m in the central sector and abruptly thins to <8 m towards the eastern and western sectors (Figure 3). This increase in thickness coincides with deeper erosion on the basal surface.

Unit 2 is characterised by a matrix-supported medium-grained muddy sandstone to sandy mudstone and is very poorly sorted throughout, ungraded, and with a chaotic distribution of outsized

clasts (F14; Figure 5). Clasts range in character and size from granular quartz grains and rounded volcanic epiclasts to much larger megaclasts (>4.1–140 m long) (Hodgson et al., 2019) of either conglomeratic or heterolithic lithology (Figures 2C,D, 4F, 5). The chaotic distribution of polymictic clast encased into a muddy sand matrix is responsible for the block-in-matrix fabric (e.g. Ogata et al., 2012). Typically, conglomeratic megaclasts are rounded, elongated and weakly deformed (Figures 2D, 4F,G) and are clast-supported, with well-rounded to sub-angular clasts (0.03–1 m diameter) and fragments of thick-shelled bivalves (oysters; Figure 4D). These oyster-bearing conglomeratic megaclasts are preferentially located near the base of Unit 2 (Figures 2C,D, 3B). In contrast, heterolithic megaclasts are angular and characterised by internally folded packages of planar laminated and normally graded thin-bedded material (Figures 2C, 5) and preferentially distributed toward the top of Unit 2 (Figures 3, 5). This heterogeneity promotes a homogeneous matrix-rich texture in the middle division.

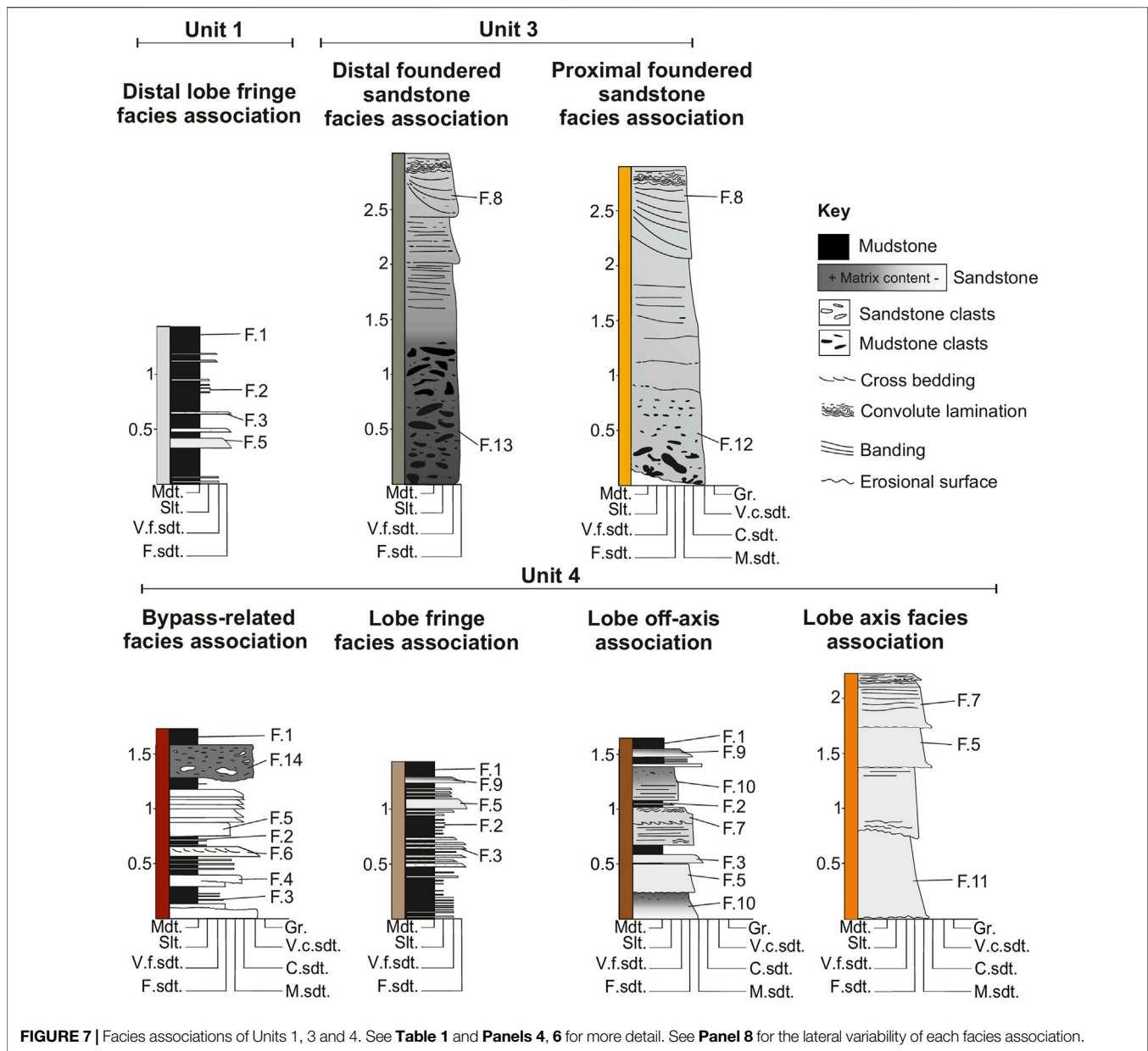
Apart from the irregular basal contact of Unit 2, thickness changes within the unit are strongly controlled by the rugose upper surface. Kilometre-scale wavelength (1–3 km) and metre-scale amplitudes (0.5–8 m) are responsible for a complex supra debrite topography.

Interpretation: The sedimentary characteristics of this unit, such as the chaotic distribution of (mega)clast floating onto a



muddy sandstone to sandy mudstone matrix, suggest near-instantaneous deposition from a flow with high yield strength and buoyant support that could transport clasts up to 140 m long (Stow and Johansson, 2000; Mulder and Alexander, 2001). Using Datum A, the debris formed a long-wavelength mounded top (**Figure 3**), attributed to the parental flow's cohesive nature and en-masse freezing. We interpret Unit 2 as a cohesive debris flow deposit (Talling et al., 2012). The ramp and flat geometry at the base of Unit 2 indicate the debris flow's erosive nature (e.g., Lucente and Pini, 2003). The similarity in composition between

the heterolithic megaclasts and underlying Unit 1 suggests entrainment of deep-marine substrate blocks due to the shear stress exerted by the overriding debris flow (Van der Merwe et al., 2009; Watt et al., 2012; Ogata et al., 2014a; Hodgson et al., 2019). In contrast, the sand content in the matrix and the oyster-bearing conglomerate megaclasts suggest a shallow marine origin of the mass failure (e.g., Ogata et al., 2012). Alternatively, the megaclast bearing shells could come from the remobilization of older slope strata, including shallow-marine deposits (La Primavera Fm; Suárez and de la Cruz, 1997; Llambías and Leanza, 2005). The



two distinct megaclast sources suggest long-distance transport of clasts and flow bulking through local substrate entrainment (e.g., Sobiesiak et al., 2016).

Unit 3

Description: Unit 3 (0–4 m thick) is composed of thick sandstone beds (0.5–2 m) with sharp, irregular concave-up bases and abrupt pinchout terminations, which result in a disconnected distribution of packages of wedge-shaped sandstone bodies (**Figure 6**) (see architecture section). Unit 3 is only present where Unit 2 is relatively thin (in the eastern-central and western sectors) and is absent in the central region where Unit 2 shows its maximum thickness (**Figure 3**). Where Unit 3 is absent, Unit 4 overlies Unit 2 (**Figure 3**). Unit 3 comprises bed

types characterised by two main amalgamated divisions (lower and upper divisions) with some grain size breaks lacking any mudstone- and siltstone-rich bounding intervals (**Figures 6A, 7**). The basal interface of these sandstone bodies shows centimetre-scale undulations characterised by abundant load casts, semi-detached ball structures, and mudstone intrusions (diapirs and injectites) originating from Unit 2 (**Figure 6G**).

Two different types of thick-bedded amalgamated sandstone facies dominate the lower division, which varies along the transect. Grain-size breaks define amalgamation surfaces within sandstones. In the western sector, and more rarely in the eastern sector, the lower divisions are characterised by thick-bedded (0.5–2 m thick), structureless, weakly normally-graded, moderately-to poorly-sorted sandstones (F12). At bed bases,

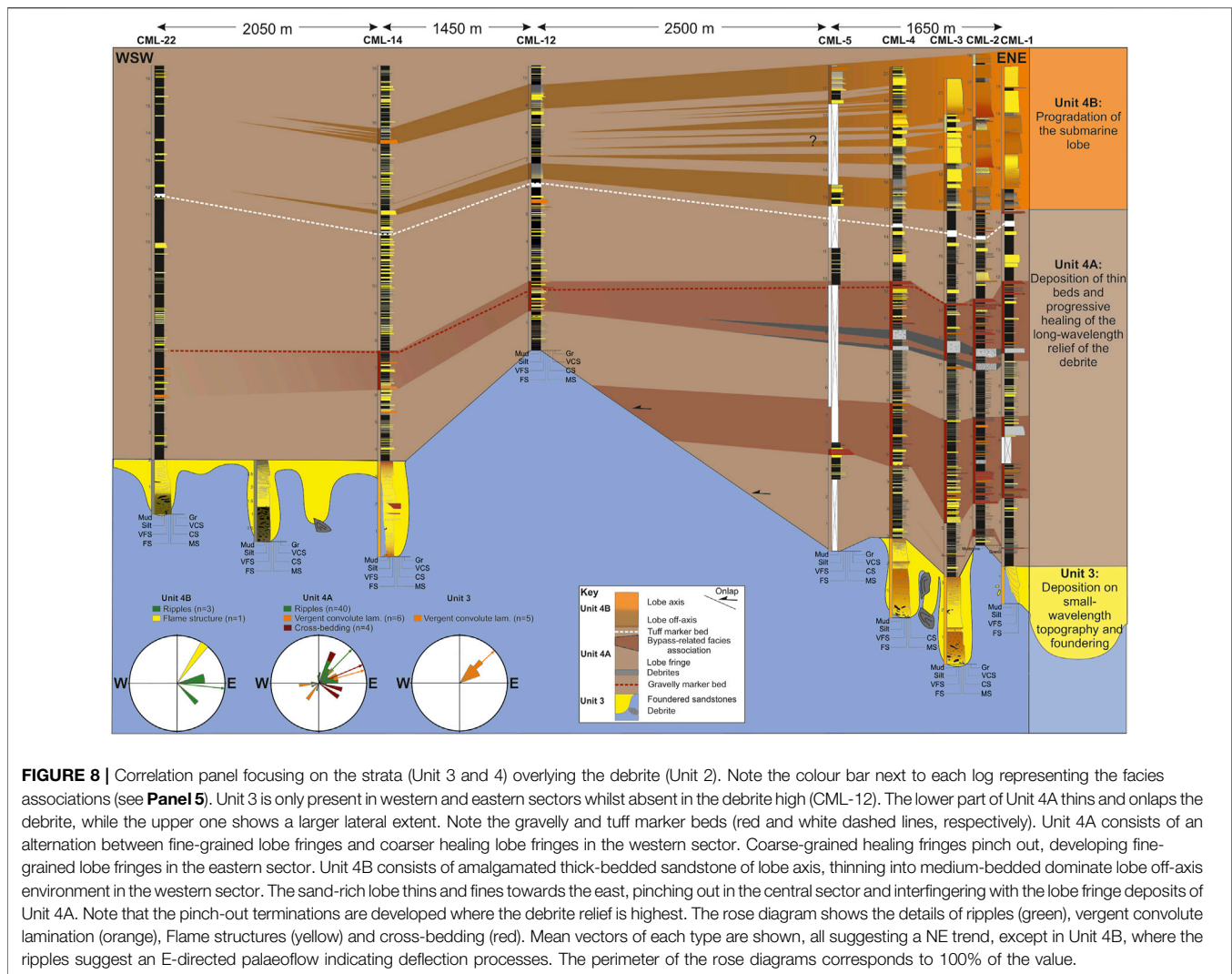


FIGURE 8 | Correlation panel focusing on the strata (Unit 3 and 4) overlying the debris (Unit 2). Note the colour bar next to each log representing the facies associations (see **Panel 5**). Unit 3 is only present in western and eastern sectors whilst absent in the debris high (CML-12). The lower part of Unit 4A thins and onlaps the debris, while the upper one shows a larger lateral extent. Note the gravely and tuff marker beds (red and white dashed lines, respectively). Unit 4A consists of an alternation between fine-grained lobe fringes and coarser healing lobe fringes in the western sector. Coarse-grained healing fringes pinch out, developing fine-grained lobe fringes in the eastern sector. Unit 4B consists of amalgamated thick-bedded sandstone of lobe axis, thinning into medium-bedded dominate lobe off-axis environment in the western sector. The sand-rich lobe thins and fines towards the east, pinching out in the central sector and interfingering with the lobe fringe deposits of Unit 4A. Note that the pinch-out terminations are developed where the debris relief is highest. The rose diagram shows the details of ripples (green), vergent convolute lamination (orange), Flame structures (yellow) and cross-bedding (red). Mean vectors of each type are shown, all suggesting a NE trend, except in Unit 4B, where the ripples suggest an E-directed palaeoflow indicating deflection processes. The perimeter of the rose diagrams corresponds to 100% of the value.

these sandstones comprise well-rounded (0.1–1 m diameter) mudstone clasts of low-sphericity and diffuse boundaries (mudstone clast type A), which show a coarse tail grading (**Figures 6A,G**). Locally, in the eastern sector, lower divisions of these sandstone bodies comprise thick-bedded, structureless, very poorly-sorted, more argillaceous sandstones with abundant mudstone clasts (0.1–1 m diameter) with very diffuse boundaries (mudstone clast type A), which are ungraded and randomly orientated (F13) throughout the encasing matrix (**Figure 5F**).

The lower division of Unit 3 sandstone bodies are overlain by an upper division (up to 2 m thick), which comprises coarse to very fine-grained, normally graded, moderately-to poorly-sorted sandstones (0.5–1.7 m) (**Figure 6A**). Banding can be developed throughout the bed or overlying a structureless division (**Figure 6A**). The banding is characterised by an alternation between lighter matrix-poor bands and darker matrix-rich bands that comprise bedding parallel millimetric mudstone clast with sharp boundaries (mudstone clast type B) (F8; **Figure 6C**). Contacts between bands are diffuse (**Figures 6B,F**). The spacing between the individual bands (0.5–2 cm)

increases from the margin to central parts of the sandstone body (**Figure 8**), commonly showing rotation (**Figure 6E**). These sandstones develop symmetrical and asymmetrical convolute lamination at bed tops (predominant vergence towards NE; **Figure 6D**). Decimetre-scale long and centimetre-scale thick mudstone injections can be observed within this division (**Figure 6B**).

Interpretation: The wedge-shaped and deformed concave-up basal contacts of the sandstone bodies beds in Unit 3 are interpreted to reflect the interaction with the rugose upper surface and syn-sedimentary foundering of sand into the underlying mud-rich debris (**Figures 6, 9**). Foundering is driven by instability due to the density contrast between the sand deposited above a less dense debris (density loading) and lateral changes in sediment load (uneven loading) (Owen, 1987, 2003) produced by the short-wavelength rugosity of the upper surface.

The lack of sedimentary structures in the lower divisions of bed types recognised in Unit 3 is interpreted as a product of hindered settling from highly-concentrated gravity-flows,

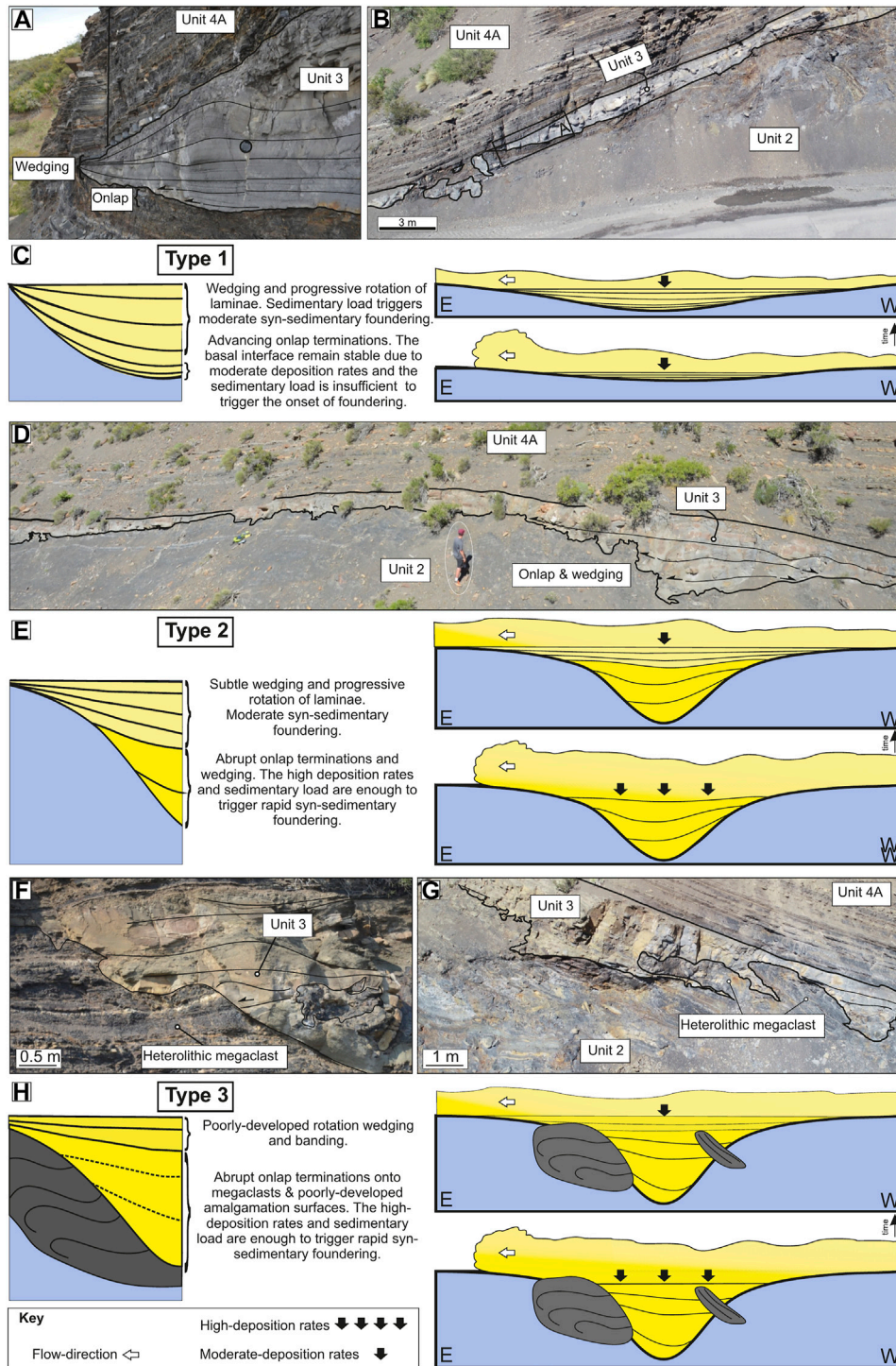


FIGURE 9 | Illustrative diagram of founded sandstone architecture and a model for their development. Type 1: **(A)** Thin-bedded sandstone with onlap termination at the base, indicating interaction with inherited relief and wedging associated with the syn-depositional foundering. **(B)** Bodies wedge smoothly, forming lenticular bodies with flat tops. Note the location of A) indicated by a black rectangle. **(C)** Sketch of the architecture and evolutionary model of Type 1 architecture: Initial deposition is insufficient to trigger the foundering. Type 2: **(D)** Thick-bedded founded sandstones with associated thinner margins. Central parts are composed of sandstones deposited by high-density turbidity currents, whereas the thinner margins are sandstones interpreted as being deposited under more fluidal sediment gravity flows (Transitional flows). **(E)** Sketch of the architecture and evolutionary model of Type 2 architecture: Initial deposition is enough to trigger the foundering. Type 3: **(F, G)** The shape of the thick-bedded sandstone bodies depends on the size and geometry of the thin-bedded megaclast. See **Panel 5** for more detail. **(H)** Sketch of the architecture and evolutionary model of Type 2 architecture: While foundering, the sandstone might be protruded by the megaclast due to its higher competence than the surrounding debrite matrix.

resulting in turbulence damping and rapid deposition (Talling et al., 2012), inhibiting any period of traction (Sumner et al., 2008). The normally-graded lower divisions were produced by incremental layer-by-layer deposition from high concentration gravity flows, such as high-density turbidity currents (sensu Lowe, 1982). In contrast, the thick-bedded argillaceous sandstones with ungraded mudstone clasts observed in the distal areas (eastern sector) are interpreted as moderate-strength cohesive debrites (sensu Talling et al., 2012). The decimetre-scale mudstone clasts (type A) were transported due to the matrix strength of the debris flows and their positive buoyancy with respect to the encasing matrix.

The lateral facies transition from high-density turbidites to moderate strength cohesive debrite suggest a flow transformation due to the entrainment of cohesive material from the underlying debrite (e.g., Kane and Pontén, 2012; Baker et al., 2017). The unconsolidated state of the debrite might have enhanced the substrate entrainment of decimetre-scale mudstone clasts (type A) and disaggregation (as indicated by the diffuse boundaries: **Figure 6G**), increasing the amount of mud and, therefore, the cohesiveness of the flow. Based on facies juxtaposition, the foundered sandstones can be subdivided into two different facies associations: 1) proximal and 2) distal, foundered sandstones facies associations (**Figure 7**). Both high-density turbidites and moderate strength cohesive debrites are characterised by rapid deposition (incremental deposition and en masse freezing, respectively), triggering the liquefaction of the fluid-saturated and unconsolidated upper surface of the debrite and foundering of sand (**Figure 9**). The undulations of the concave-up basal interface reflect complex interactions with the substrate: as the denser sand sank into the fluid-saturated muddy substrate, the buoyancy of mud promoted the syn- to post-depositional intrusion (mud diapirs and injectites) of the substrate into sandstones. The most advanced stage of foundering is observed when detached sand-balls develop (**Figure 5**; Owen, 2003; Tinterri et al., 2016).

In contrast, the banded sandstone characteristic of the upper divisions is interpreted to be formed under episodic near-bed turbulence damping at high rates of deposition (Lowe and Guy, 2000). The juxtaposition of the banded sandstones over the mudstone-clast bearing sandstones of the lower divisions suggests highly stratified flows, mixing and upwards transfer of centimetre-scale mudstone clast (type B) and the cohesive material from the disaggregation of the entrained decimeter-scale mudstone clast (type A). This enrichment in cohesive clayey material triggered the periodic suppression of turbulence and, therefore, banding development. The banding passes into convolute laminations towards the top, indicating moderate rates of deposition. The vergence of convoluted laminations suggests a syn-sedimentary shear-stress exerted by the overriding flow (McClelland et al., 2011; Butler et al., 2016) and flow-rebound produced by the underlying debrite relief (e.g., Tinterri et al., 2016).

Unit 4

Description: Unit 4 (10–27.3 m thick) has a sharp and concordant contact with the underlying Unit 2 and Unit 3

(**Figure 3**). It comprises two subunits: a lower heterolithic interval (Unit 4A) and an upper sandstone-prone interval (Unit 4B; **Figure 2C**).

Unit 4A is thin- to medium-bedded (0.01–0.5 m; **Figure 4H**) heterolithic succession (F1, F2, F3 and F5) with a maximum thickness of 22 m, thinning to 8 m in the central sector above where Unit 2 is thickest (**Figure 3**). Most of the thin-beds (0.01–0.1 m thick) are fine- to medium-grained normally-graded sandstones, matrix-poor, moderately well-sorted, and structureless with common planar-parallel lamination and/or starved-ripple lamination near bed tops (F3; **Figure 4C**). Palaeocurrent measurement shows a consistent flow trend towards the NE (**Figure 9**). Unit 4A also comprises coarse- to granular normal-graded sandstones, relatively low matrix content with common grain size-breaks (0.07–0.2 m thick), erosive bases and sharp-planar tops (F4; **Figure 4D**) and two medium-bedded matrix-supported conglomerates with sandstone clasts (F14; 0.25 and 0.35 m thick, respectively) that pinch out towards the central sector (**Figure 8**). One of these thin gravelly beds, which lacks any lateral thinning or fining trend (**Figure 4I**), was traced across the exposure (gravelly marker bed; dashed red line in **Figure 8**). In addition, a 0.15 m thick tuff layer (**Figure 4J**) was also used for correlation purposes (tuff marker bed; dashed white line in **Figure 3**). The medium-bedded sandstones (0.1–0.5 m thick) are structureless, ungraded, with planar-parallel and convolute lamination at bed tops, except one that shows cross-bedding (F6; **Figure 4D**). These sandstones have sharp bed bases and tops and lack mudstone clasts. In the eastern sector, Unit 4A is dominated by thin- to medium-bedded heterolithic succession that lacks any gravelly (F5) or matrix-supported conglomerate beds (F14).

Unit 4B (5.7 m thick in the western sector) thins eastwards along a 4.3 km transect until it pinches out, where Unit 2 is thickest (**Figure 3**). In the western sector, it dominantly comprises medium- (F5; **Figure 4K**) to thick-bedded sandstones (F11; **Figure 4K**), with less common “bipartite” sandstone beds (F9 and F10) composed of a matrix-poor lower division and a matrix-rich upper division with mudstone clasts. Conformable bases and sharp tops characterise the thick-bedded sandstones (0.5–1.2 m). Where the thick-bedded sandstones are not amalgamated and are intercalated centimetre-thick beds of fine-grained material (F1 and F2), bed bases are loaded locally. The thick-bedded sandstones are normally graded from medium to fine sand, well-sorted with rare centimetric mudstone clasts at the bed top. Soft-sediment deformation structures, such as centimetre-scale flames with NE vergence, are also common at bed bases and along amalgamation surfaces (**Figure 4L**). Banded sandstones are medium-bedded (0.1–0.5 m), fine- to medium-grained, and characterised by alternating between light- and dark-coloured bands, ranging from 0.2 to 2 cm thick (F7; **Figure 4L**). Both band types show a similar maximum grain size, although the darker bands are matrix-rich, and light bands are matrix-poor. Banding is generally sub-parallel to bedding. Although banded sandstones are more commonly associated with thick-bedded structureless sandstones, the banded sandstones can be individual event beds, with banding above the structureless basal division. The medium-bedded bipartite sandstone beds (0.1–0.5 m) consist of a

medium-grained, matrix-poor and structureless lower division, which is overlain by a fine-grained matrix-rich upper division characterised by poor sorting and abundant mudstone clasts (0.05–0.3 m) with low sphericity and variable roundness (F9 and F10; **Figure 4M**). The lower and upper divisions show a gradual upwards increase in matrix content rather than across a sharp boundary. When Unit 4B is traced eastwards towards the central sector, the sandstone package transitions into a few thin-beds (0.1 m thick) of weakly graded, very poorly-sorted matrix-rich sandstone, lacking the mudstone clasts observed in western areas. Unit 4B is absent in the eastern sector.

Interpretation: In Unit 4A, the thin sandstone beds showing planar and cross ripple laminations support an interpretation as low-to medium-density turbidites (Talling et al., 2012). The starved-ripple lamination observed in thin-bedded sandstones is interpreted as the reworking of sand deposited by dilute flows with low sedimentation rates (Talling et al., 2007; Jobe et al., 2012). The intercalation of thin-bedded sandstones with finer-grained deposits suggests a lobe fringe environment (Lobe fringe facies association, **Figure 5**) (Prélat et al., 2009; Spychala et al., 2017b). The abundant coarse-grained to gravelly thin-bedded sandstones in the western sector record intermittent energetic coarse-grained flows, suggesting sporadic sediment bypass processes (Stevenson et al., 2015). However, the low matrix content within the granular beds suggests a sediment source area where only coarse-to granular grain size was available. The intercalation of such different facies suggests the juxtaposition of depositional environments of contrasting energy and/or different sediment sources. Either scenario could be possible given the complex sediment routing patterns and multiple transverse or axial sources available in the Neuquén Basin during the early post-rift setting (Vicente, 2005; Privat et al., 2021) and by analogy to other post-rift settings (e.g., Lien, 2005; Fugelli and Olsen, 2007; Hansen et al., 2021). The mass failure would trigger a new coarse-grained source due to slide scar position and geometry, promoting intermittent sand supply to an otherwise sand-starved environment (see “Origin and role of the Mass-wasting process as a trigger for turbidite systems development” in discussion). The downdip variability in the thickness of Unit 4A (from 22 to 8.5 m thick), reduction in gravelly sandstone content and the stratigraphic thinning between the granular marker bed (red dashed line in correlation) and the top debrite (Unit 2) reveals the existence of subtle relief on the debrite surface (**Figure 3B**). Furthermore, the two poorly sorted ungraded muddy sandstones, which are interpreted to be debrites due to their chaotic distribution of clast within the argillaceous matrix, also pinch out towards the central sector. The ripples and convolute laminae with SW vergence (**Figure 3**) contrast with the consistent NE paleoflow, suggesting local flow deflection (cf. Tinterri et al., 2016) in the central sector, where the debrite relief is highest, indicating the interaction between sediment gravity-flows and the upper surface of the debrite.

Massive medium-to thick-bedded deposits of Unit 4B are interpreted as high-density turbidites formed by incremental layer-by-layer deposition with high aggradation rates (Kneller and Branney, 1995), interpreted to represent proximal lobe axis

environments (lobe axis facies association; **Figure 5**) (e.g., Prélat et al., 2009; Kane et al., 2017). The location of these facies in the westernmost sector, and the palaeoflow measurements, suggests that the western sector was relatively proximal. Banded sandstones represent the deposits of mud-rich transitional flows formed by tractional reworking (Stevenson et al., 2020). The bipartite beds consisting of a basal structureless to planar laminated sandstone division, overlain by a linked mudstone clast-rich upper division are interpreted as hybrid event beds (HEBs), formed from transitional flows deposited under high-deceleration rates (Haughton et al., 2009; Hodgson, 2009; Kane and Pontén, 2012) in more distal environments than the banded sandstones (Stevenson et al., 2020). The gradual and diffuse boundary between the basal turbidite and the upper debrite suggest vertical segregation of particles within the cohesive flow (Kane et al., 2017). The facies evolution of Unit 4B from proximal (western sector) to distal (eastern sector) of thick-bedded sandstones into hybrid event beds likely represents the downdip transition from lobe-axis/off-axis environments (lobe axis facies association: **Figure 5**) (sensu Prélat et al., 2009) into lobe-fringe environments (lobe fringe facies association; **Figure 5**) (e.g., Spychala et al., 2017a; Kane et al., 2017), persisting until the frontal/oblique pinchout (e.g. Hansen et al., 2019).

DEPOSITIONAL ARCHITECTURE OF THE DEBRITE AND OVERLYING UNITS

Large Scale Architecture: Debrite Relief

Using Datum A (“Burro” marker bed), the upper surface of the >9.6 km long debrite forms a broad convex-up relief that reaches a maximum in the central section coincident with the deepest incision (at least 22.5 m of erosional relief; **Figure 3B**). The spatial association of the thickest part of the debrite with the deepest incision support a genetic link between the geometry of the flat-ramp-flat shaped basal shear zone and the mounded top. The morphology of the basal surface can buttress material translated downslope and develop positive topographic features, such as pressure ridges (Moscardelli et al., 2006; Bull et al., 2009). Bed-by-bed correlation within Unit 4A shows that where the upper surface of the debrite develops the highest relief (~8 m of positive relief with respect to the western sector), Unit 3 is absent, and it is overlain by Unit 4A (**Figure 3**), showing a laterally continuous stratigraphic interval with metre-scale thickness variations (**Figure 8**). Unit 4A thins from 22 m (CML-1) and 13 m (CML-2) to 6 m (CML-12) across the highest part of the debrite (**Figure 3B**). The lower part of Unit 4A pinches out in the central sector, developing onlaps of individual beds, and supporting the existence of a gentle relief (Bakke et al., 2013; Soutter et al., 2019). In contrast, the upper part of Unit 4A shows tabular architecture with a lateral continuity of over 7 km.

Unit 4A is overlain by Unit 4B, which shows a progressive thinning of the submarine lobe from the western to the central sector over 5.6 km, from 5.7 m (CML-3) to 1.7 m (CML-12) and 1 m (CML-14) with a mean thinning rate of 0.9 m/km. The

submarine lobe pinches out between CML-14 and CML-22 (<2 km), interfingering with unit 4A (**Figure 3B**). The lack of onlap geometries against underlying deposits and subtle thinning rates consistent with unconfined settings (e.g., Prélat et al., 2009) suggests a lack of a pronounced pre-existing relief. However, the coincidence of lobe pinch-out in the area where the debrite relief is highest and where the underlying Unit 4A is thinnest might reflect subtle residual relief.

Small-Scale Architecture: Foundered Sandstones

The steeply-dipping unconformable base, internal deformation and abrupt thickness changes of Unit 3 sandstones contrast with their flat and conformable tops (see stereoplots in **Figure 6**). These sandstone bodies can be subdivided into three different types by their architecture.

Type 1

Description: The thinner founded sandstone bodies range between 0.5 and 2 m thick and are only formed by the banded sandstones (**Figures 9A,B**). They are characterised by 5–25 m wide lenticular shapes, with thickness/width ratios varying from 1:5 to 1:18. These sandstone bodies show relatively constant thinning rates (~0.25 cm/m) towards their pinch outs. They are characterised by: 1) advancing onlap terminations onto Unit 2 at the base, and a vertical change into; 2) progressive rotation of laminae and the wedging of the sandstones (**Figure 9C**).

Interpretation: The onlap termination indicates the interaction between the parental sediment gravity flow and pre-existing debrite-related relief (e.g., Bakke et al., 2013), and the sediment load was insufficient to trigger the soft-sediment deformation along the upper surface. In contrast, the overlying rotation and wedging represent growth strata associated with the syn-sedimentary foundering. This juxtaposition of terminations indicates that foundering did not start since the onset of deposition of sand due to insufficient stress to trigger the soft-sediment deformation. This supports an incremental layer-by-layer deposition of these sandstones rather than the freezing of the parental flow.

Type 2

Description: Thick-bedded founded sandstones (up to 4 m thick) are characterised by irregular stepped bases and abrupt thickness variations (up to 2 m thinning over 1 m laterally) (**Figure 9D**). They are composed by the juxtaposition of two different divisions: 1) lower and 2) upper divisions (**Figure 9E**). The lower divisions comprise structureless sandstones with poorly-developed amalgamation surfaces (F12 or F13). They rarely exceed 10 m laterally and 3 m in thickness (thickness/width 1:2 to 2:1) and are characterised by both abrupt onlaps terminations and wedging. In contrast, the upper divisions are characterised by banded sandstones (F8), which are more laterally extensive than the underlying division, with a maximum length of 50 m and rarely exceed 1 m in thickness, and thin laterally towards margins (thickness/width 1:10).

Interpretation: The coexistence of onlaps terminations and wedging indicate that the foundering began at the onset of deposition and the existence of pre-existing topography along the upper surface. The sediment load was enough to trigger the foundering because the debrite relief strongly influenced the initial high-concentration flows, which promoted a loss in flow capacity and deposition under high aggradation rates. The rapid deposition and foundering are responsible for the poorly-developed onlap terminations and amalgamation surfaces. The deposition of lower division deposits promoted a reduction in debrite rugosity due to the infilling of topographic lows, enabling the deposition of laterally more extensive deposits. The rotation and wedging in the banding of the upper division is less well developed than in Type 1 sandstone bodies. This suggests a progressive reduction in syn-sedimentary deformation and an increase in seafloor stability (e.g., Owen, 1987, 2003).

Type 3

Description: These sandstone bodies show similar facies juxtaposition as in Type 2. In this case, the sandstones terminate against heterolithic megaclasts due to their preferential location towards the top of the debrite (**Figures 5, 9F**). In these cases, the geometries of the founded sandstones diverge from the concave-up geometry, dependent on the shape of the megaclast. Some megaclasts disconnect bodies laterally, whereas others only impact the base, with the top part of the sandstones undisturbed (**Figure 9G**).

Interpretation: The fluid-saturated matrix and rigid megaclast respond differently to the shear stress exerted by the deposition of sand creating. This differential compaction (Ogata et al., 2014b) controls the architecture of the founded sandstones, creating complex bodies (**Figure 9H**).

DISCUSSION

Basal Shear Zone and Impact on the Substrate

As submarine landslides travel across the seafloor, they exert shear stress on the substrate, coupled with significant overpressure (Bull et al., 2009; Hodgson et al., 2019; Payros and Pujalte, 2019). This leads to substrate entrainment (Eggenhuisen et al., 2011; Hodgson et al., 2019) and/or deformation (Butler and McCaffrey, 2010; Watt et al., 2012; Dakin et al., 2013; Ogata et al., 2014b). The debris flow (Unit 2) incised at least 22.5 m into the substrate (Unit 1; **Figure 3**). In the central sector, the basal shear surface forms ramps (up to 800 m long, >2°) and flats (up to 1,550 m long; **Figure 3B**; between the logs CML-9 and CML-10) (see Lucente and Pini, 2003; Frey Martínez et al., 2005 for flat-ramp-flat geometry). The stress applied to the substrate during the emplacement is accommodated by both stratigraphic intervals consisting of deformed packages (basal shear-zone) and interfaces consisting on a plane (basal shear-surface) (Alves and Lourenço, 2010), such as the discrete basal shear zone located in upper Unit 1. The absence of contractional features in the deposits underlying Unit 1 supports the deformation as the result of the shear stress produced by the

emplacement of the debrite rather than tectonism. The basal shear zone has variable thickness and deformation styles. It is absent in the western sector, whereas erosion and deformed intervals record a high degree of basal shear stress in the central sector (**Figure 3B**). In the central sector, the deformed package (up to 10 m thick) is characterised by decametre-scale thrusts with metre-scale offsets and drag folding (**Figure 4B**). The predominance of imbricate thrusting over folding, and lack of internal disaggregation within the package, indicate competent substrate rheology (e.g., Van Der Merwe et al., 2011). The eastward vergence of the compressional structures (**Figure 4B**) indicates an eastward emplacement direction for the debris flow (Twiss and Moores, 1992), consistent with the palaeoflow indicators in the bounding strata.

The thrusting is attributed to bulldozing by the entrenched debris flow (e.g., Jackson, 2011; Hodgson et al., 2019; Payros and Pujalte, 2019), representing the initial stage of substrate entrainment. Entrainment of megaclasts into a debris flow has been reported in other systems in the subsurface (Moscardelli et al., 2006; Alves and Cartwright, 2009; Sawyer et al., 2009; Dakin et al., 2013; Ortiz-Karppf et al., 2015; Soutter et al., 2018; Nwoko et al., 2020a) and more rarely at outcrop (Ogata et al., 2014b; Sobiesiak et al., 2016; Hodgson et al., 2019; Cumberpatch et al., 2021). The progressive increase in thickness and degree of strain along the basal shear zone of Unit 2 and the enrichment in rafted heterolithic megaclasts (**Figures 3B, 5**) suggest downdip evolution of the debris flow, which might have affected the parental debris flow rheology (e.g., Hodgson et al., 2019; Payros and Pujalte, 2019) and bulking of the flow (Gee et al., 2006; Alves and Cartwright, 2009; Butler and McCaffrey, 2010; Hodgson et al., 2019). The preferential location of heterolithic megaclast towards the top of Unit 2 might be related to internal granular convection cells created along with the debris flow, enhanced by the buoyancy of less dense rafted megaclast compared to debrite matrix (Hodgson et al., 2019) and kinetic sieving (Legros, 2002). In contrast, conglomerate megaclasts are always found at the base of the debrite due to their higher density than the surrounding debrite matrix.

Dynamic Debrite Topography and Impact on Overlying Strata

The absence of Unit 3 sandstones over the thickest part of the debrite suggests that the sediment gravity flows were strongly stratified and influenced by the debrite relief (**Figure 8**). The sandstone bodies are also disconnected at finer scales, revealing short wavelength (metre-scale) and amplitude (decimetre-scale) rugosity on the debrite surface. The existence of simultaneous short wavelength and amplitude rugosity superimposed on a large-scale wavelength relief on the upper surface of an MTD has also been reported by Armitage et al. (2009), defined as “surface-topography hierarchy,” in the Cretaceous Tres Pasos Formation at the Sierra Contreras (Chile) and by Fairweather (2014) in Carboniferous Paganzo Basin at Cerro Bola (Argentina). In this study, the deposition of sand in pre-existing lows filled the short-wavelength rugosity and triggered the loading of individual sandstone bodies onto the mud-rich

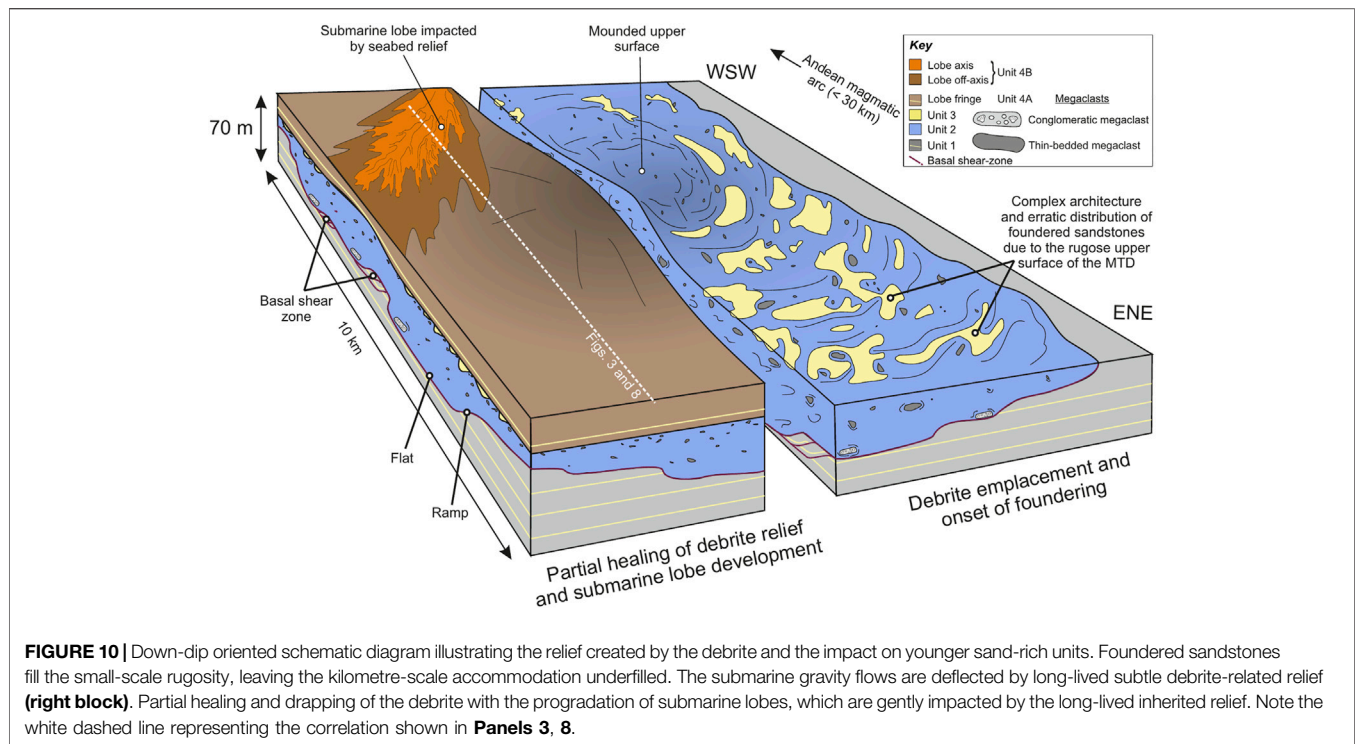
debrite (See “Small-scale architecture: Foundered sandstones” sections), leaving the large-scale relief underfilled (**Figures 3, 8**). The foundering process is evidence of substrate liquefaction and highlights the dynamic interface between the debrite and subsequent flows and their deposits. A similar scenario was proposed by Van der Merwe et al. (2009), Van der Merwe et al. (2011) in the Vischkuil Formation in the Laingsburg depocentre (Karoo Basin).

The ability of supra MTD rugosity to pond turbidity currents travelling across their upper surface is a well-known phenomenon (Kneller et al., 2016). However, the presence of Unit 3 founded sandstones up-dip and down-dip of the debrite high (**Figure 3B**), and its consistent NE paleocurrent trend, suggest connected sediment transport routes across the debrite with no evidence of flow ponding or stripping (e.g. Armitage et al., 2009; Fairweather, 2014). The highly-stratified grown-hugging parental flows of Unit 3 would have been ponded in proximal parts (western sector) if a fully enclosing topography existed given their reduced ability to surmount obstacles (Al-Ja’Aidi et al., 2004; Bakke et al., 2013), resulting in sand starvation over the debrite in distal settings (Sinclair and Tomasso, 2002; Kneller et al., 2016). The overlying Unit 4A can be traced laterally across the study area, with metre-scale thinning where the debrite is thickest (see CML-12; **Figure 3**). Apart from this, the advancing onlap geometries of the thin beds and the divergence in the overall NE-orientated paleocurrents (rose diagram Unit 4; **Figure 3**) indicate the progressive healing of the large-scale wavelength debrite relief, with some deflection of turbidity currents (**Figure 10**).

The thin sandstone beds of the upper part of Unit 4A healed the debrite high. However, the gravelly beds thin and fine from proximal to distal areas (western to eastern sectors), and the two debrites pinch out in proximal areas (western sector), suggesting subtle remnant topography (**Figure 8**). The different lateral continuity of individual beds is explained by different rheologies of individual sediment gravity flows, which affect the flow efficiency (Al Ja’Aidi et al., 2004). Cohesive debris flows are more influenced by irregular relief, while low-density turbidity currents are less affected by seafloor topography (Bakke et al., 2013; Soutter et al., 2019). This suggests that laterally continuous thick accumulations of lobe fringe deposits can develop on gentle topographies, while the submarine lobes’ axial parts were restricted to lower relief areas. The interaction of thin-bedded turbidites successions with gentle topography has also been reported in other deep-water settings (i.e., “aggradational lobe fringes”; Spsychala et al., 2017b). The deposition of lobe fringe successions reduced confinement, which enabled the deposition of the Unit 4B submarine lobe.

The submarine lobe is characterised by a progressive thinning and fining, developing pinch-out geometries and interfingering with Unit 4A in the area where the relief of the debrite is highest. The development of pinch-out geometries over the areas where the debrite shows a mounded relief and where the Unit 4A onlaps and thins suggests that the relief was not wholly healed with the deposition of Unit 4A and affected the parental flows of Unit 4B.

One explanation is that the exposure exhumes the Unit 4B lobe obliquely, with the medium-to thick-bedded lobe axis



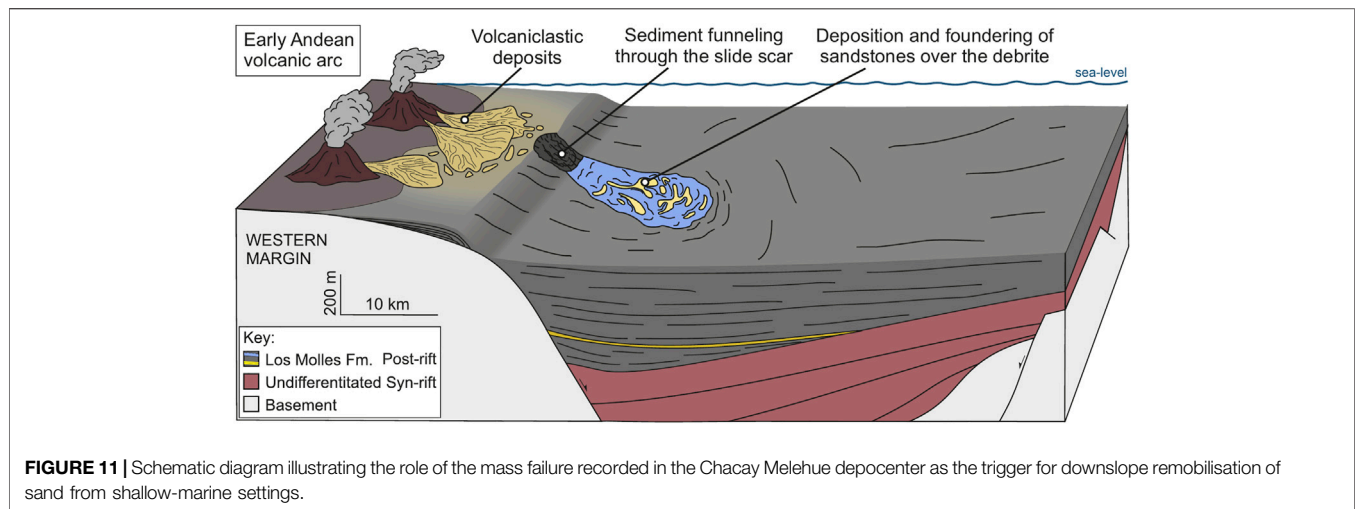
deposits in the westernmost sector (CML-1 to CML-4) transitioning into an HEB-dominated fringe, being highly impacted by gentle seafloor topography (Soutter et al., 2019; Privat et al., 2021). Alternatively, the seafloor relief could have promoted the modification of flow pathways and deflection of flows, thus changing the downdip orientation (**Figure 8**). All these scenarios suggest a confined and uncontained (see Southern et al., 2015) lobe-type depositional system. The precise dispersal pattern of the flows remains unknown due to the outcrop limitations. Nonetheless, the documented stratigraphic evolution reveals that long-lived debrite relief and progressive healing by deposition of aggradational lobe fringes enabled the progradation of sand-rich submarine lobe, albeit with changes in flow rheology the bed style and element-scale pinchout (**Figure 8**).

Another explanation is that the debrite relief in the central sector might have been rejuvenated through volume changes in the debrite due to differential compaction by loading the lobe itself in the proximal sector. However, it seems unlikely that the deposition of a 5.7 m thick lobe could promote a volume loss in an 8–47 m thick debrite, given that both units are separated by 8–22 m thick thin-bedded interval. In contrast, another two hypotheses are deemed more plausible; fluid loss and fault-controlled mechanical subsidence. Fluid loss-controlled evacuation could have promoted differential subsidence of the upper surface of the debrite and overlying units (e.g., Browne et al., 2020). Alternatively, given the early post-rift setting, mechanical subsidence by an east-facing and N-S striking fault (Maceda and Figueroa, 1995) could have generated more

accommodation in the western part of the study area (see Cristallini et al., 2006). However, this implies a very localised and rapid reactivation, and there is no other evidence for post-rift tectonism identified.

Origin and Role of the Mass-Wasting Process as a Trigger for Turbidite Systems Development

The emplacement of the >9.6 km long and erosional debrite in the Chacay Melehue depocentre reflects an abrupt change in sedimentation patterns, which were previously dominated by dilute mud-rich flows (Unit 1). The first significant sand influxes in the depocentre for ~6 Myr since the Aalenian (interval II of Gulisano and Gutiérrez Pleimling, 1995) are recorded by the sand-rich deposits (Unit 3) immediately overlying the debrite (**Figure 10**). The juxtaposition of sand-rich turbidites over debrites (metres to hundreds of meters thick) have been reported in other systems (Kleverlaan, 1987; Labaume et al., 1987; Payros et al., 1999; Fallgatter et al., 2017). These authors suggest that the debris flow underwent a period of mixing with ambient water, leading to the generation of an overriding co-genetic turbidity current. The foundering phenomenon reported here reveals a close spatiotemporal relationship between the debrite emplacement (Unit 2) and overlying sandstone deposition (Unit 3). An alternative mechanism is that the mass-failure event altered the basin margin physiography such that a sand source was captured. Mass-wasting processes responsible for the evacuation of material from shelf edge and upper slope areas alter the bathymetric configuration of basin



margins and promote the funnelling of sediment stored in shallow marine environments through slide scars (e.g., Moscardelli and Wood, 2008; Kneller et al., 2016; Steventon et al., 2020) (**Figure 11**). The role played as a trigger mechanism for sand delivery into deep-water setting by the mass-wasting event is a plausible scenario given the sand-starvation recorded in the coeval deposits of Los Molles Fm along the eastern margin of the Chacay Melehue depocentre (Veiga et al., 2013).

Given the palaeoflow and kinematic indicators, the thickness patterns of the studied units (**Figure 3B**), and previous studies on sediment supply from the volcanic arc (Vicente, 2005), we propose that the mass failure originated to the west of Chacay Melehue, where a major syn-rift fault is located close to the volcanic arc (<30 km; Manceda and Figueroa, 1995; De La Cruz and Suarez, 1997; Vicente, 2005). The role of the western volcanic arc as a source area for the early post-rift sediment supply in the Chacay Melehue depocentre is supported by the southeastwards directed paleocurrents measured in the Aalenian turbidite system at the base of the Los Molles Formation (Vicente, 2005; **Figure 2**) and the abundance of pyroclastic deposits within Los Molles Formation stratigraphy (Zöllner and Amos, 1973; Rosenfeld and Volldaeimer, 1980; Gulisano and Gutiérrez Pleimling, 1995; De La Cruz and Suarez, 1997; Llambías and Leanza, 2005). The oyster-bearing conglomerate megaclast and well-rounded volcanic epiclast within the matrix of the debrite reflect long-lived reworking in shallow-marine settings prior to the mass failure, suggesting a shallow-water origin or remobilization of older slope strata, including shallow-marine deposits. This could represent the downslope transfer of sand following the collapse of reworked volcaniclastic deposits along the magmatic arc (**Figure 9**). The evolution from the initial mass-wasting sediment supply responsible for erratically distributed foundered sandstone bodies (Unit 3) to a more mature system with the subtle distribution and diversity of lobe architectural elements (Unit 4) reflects the evolution to a more organised sediment supply

system (**Figure 10**). This was abruptly superseded by a return to sand-starved conditions dominated by dilute mud-rich flows and hemipelagic deposition until the end of the Lower Callovian (Gulisano and Gutiérrez Pleimling, 1995).

CONCLUSION

We document the anatomy and architecture of a >9.6 km long exhumed debrite and show how its twofold short- and long-wavelength relief and composition provided a likely input route for the subsequent sand-rich deep-water system and influenced flow behaviour depositional patterns. The basal surface of the debrite formed ramps and steps, indicating deep incision and entrainment of the substrate that included megaclasts. The foundering of overlying sands, their resultant geometry and spatial distribution, and the down-dip increase in mud content, indicate a dynamic and rugose upper surface to the debrite and complex flow-deposit interactions. The spatial distribution of the foundered sandstones indicates ground-hugging flows and the existence of debrite relief, which was progressively but not entirely healed by the submarine lobe. However, the architecture and facies distribution of the submarine lobe and their parental flows were still impacted by the long-lived, possibly rejuvenated, debrite-related topography.

The debrite emplacement coincided with an abrupt change in sediment supply to the Chacay Melehue depocentre from long-term mud-rich sedimentation to a transient sand-rich system. This change in depositional character is interpreted to have resulted from the funnelling of sediment stored in shallow marine environments to the west through a slide scar created by the debris flow, thus reconfiguring the sediment delivery pathway. Therefore, this study highlights that basin margin mass failures and their deposits play a key role in sediment dispersal patterns into deep-water settings, as well as the behaviour of subsequent sediment gravity flows travelling across their upper surface.

DATA AVAILABILITY STATEMENT

The original contributions presented in the study are included in the article/supplementary materials, further inquiries can be directed to the corresponding author.

AUTHOR CONTRIBUTIONS

AM-D took part in the data collection, analysis, figure drawing and wrote the manuscript. AP took part in data collection, suggested some modifications in figures, helped during the discussion of the main ideas and improved the writing. DH helped during the entire process (data collection, analysis and writing) and suggested to the author the potential of the outcrop belt that he had completed preliminary fieldwork with CJ, RD, YS and CS worked previously on it (Hodgson et al., 2019). IK helped with the discussion of the main ideas and contributed to the writing during the entire process. CJ, RD, YS and CS contributed to the data collection, discussion of ideas and improved the writing. EK field assisted AM-D during the

entire data collection campaign. ES contributed to the data collection and writing SF improved the writing and suggested modifications in the figures.

ACKNOWLEDGMENTS

This study is a collaboration between The University of Manchester (United Kingdom), The University of Leeds (United Kingdom), Leibniz University (Germany), The University of Liverpool (United Kingdom) and Centro de Investigaciones Geológicas (CIG) (Argentina). The authors would like to thank the local farmers of the Chacay Melehue region of Argentina for permission to carry out field studies on their land. The LOBE 3 consortium project of which this research forms a part is supported by sponsorship from Aker BP, BHP, BP, Equinor, HESS, Neptune, Petrobras, PetroChina, Total, Vår Energi and Woodside, for which the authors are grateful. We would like to thank reviewers Kei Ogata, Victoria Valdez and Mattia Marini for their thoughtful reviews, and Associate Editor Fabiano Gamberi for additional helpful comments that improved the manuscript.

REFERENCES

- Al Ja'aidi, O. S., McCaffrey, W. D., and Kneller, B. C. (2004). Factors Influencing the deposit Geometry of Experimental Turbidity Currents: Implications for Sand-Body Architecture in Confined Basins. *Geol. Soc. London, Spec. Publ.* 222, 45–58. doi:10.1144/GSL.SP.2004.222.01.04
- Allen, J. R. L. (1982). *Sedimentary Structures, Their Character and Physical Basis*, 1. Amsterdam, The Netherlands: Elsevier, 663.
- Allen, J. R. L. (1971). Instantaneous Sediment Deposition Rates Deduced from Climbing-Ripple Cross-Lamination. *J. Geol. Soc.* 127, 553–561. doi:10.1144/gsl.jgs.1971.127.06.02
- Alves, T. M., and Cartwright, J. A. (2009). Volume Balance of a Submarine Landslide in the Espírito Santo Basin, Offshore Brazil: Quantifying Seafloor Erosion, Sediment Accumulation and Depletion. *Earth Planet. Sci. Lett.* 288, 572–580. doi:10.1016/j.epsl.2009.10.020
- Alves, T. M., and Lourenço, S. D. N. (2010). Geomorphologic Features Related to Gravitational Collapse: Submarine Landsliding to Lateral Spreading on a Late Miocene-Quaternary Slope (SE Crete, Eastern Mediterranean). *Geomorphology* 123, 13–33. doi:10.1016/j.geomorph.2010.04.030
- Alves, T. M. (2015). Submarine Slide Blocks and Associated Soft-Sediment Deformation in Deep-Water Basins: A Review. *Mar. Pet. Geology*. 67, 262–285. doi:10.1016/j.marpetgeo.2015.05.010
- Armitage, D. A., Romans, B. W., Covault, J. A., and Graham, S. A. (2009). The Influence of Mass-Transport-Deposit Surface Topography on the Evolution of Turbidite Architecture: The Sierra Contreras, Tres Pasos Formation (Cretaceous), Southern Chile. *J. Sediment. Res.* 79, 287–301. doi:10.2110/jsr.2009.035
- Baas, J. H., Best, J. L., and Peakall, J. (2016). Comparing the Transitional Behaviour of Kaolinite and Bentonite Suspension Flows. *Earth Surf. Process. Landforms* 41, 1911–1921. doi:10.1002/esp.3959
- Baas, J. H., Best, J. L., and Peakall, J. (2011). Depositional Processes, Bedform Development and Hybrid Bed Formation in Rapidly Decelerated Cohesive (Mud-sand) Sediment Flows. *Sedimentology* 58, 1953–1987. doi:10.1111/j.1365-3091.2011.01247.x
- Baas, J. H., Best, J. L., Peakall, J., and Wang, M. (2009). A Phase Diagram for Turbulent, Transitional, and Laminar Clay Suspension Flows. *J. Sediment. Res.* 79, 162–183. doi:10.2110/jsr.2009.025
- Baker, M. L., Baas, J. H., Malarkey, J., Jacinto, R. S., Craig, M. J., Kane, I. A., et al. (2017). The Effect of clay Type on the Properties of Cohesive Sediment Gravity Flows and Their Deposits. *J. Sediment. Res.* 87, 1176–1195. doi:10.2110/jsr.2017.63
- Bakke, K., Kane, I. A., Martinsen, O. J., Petersen, S. A., Johansen, T. A., Hustoft, S., et al. (2013). Seismic Modeling in the Analysis of Deep-Water sandstone Termination Styles. *Bulletin* 97, 1395–1419. doi:10.1306/03041312069
- Blair, T. C., and McPherson, J. G. (1999). Grain-size and Textural Classification of Coarse Sedimentary Particles. *J. Sediment. Res.* 69, 6–19. doi:10.2110/jsr.69.6
- Boulestix, K., Poyatos-Moré, M., Hodgson, D. M., Flint, S. S., and Taylor, K. G. (2020). Fringe or Background: Characterizing Deep-Water Mudstones beyond the basin-floor Fan sandstone Pinchout. *J. Sediment. Res.* 90, 1678–1705. doi:10.2110/jsr.2020.048
- Brooks, H. L., Hodgson, D. M., Brunt, R. L., Peakall, J., and Flint, S. S. (2018). Exhumed Lateral Margins and Increasing Flow Confinement of a Submarine Landslide Complex. *Sedimentology* 65, 1067–1096. doi:10.1111/sed.12415
- Browne, G. H., Bull, S., Arnot, M. J., Boyes, A. F., King, P. R., and Helle, K. (2020). The Role of Mass Transport Deposits Contributing to Fluid Escape: Neogene Outcrop and Seismic Examples from north Taranaki, New Zealand. *Geo-mar Lett.* 40, 789–807. doi:10.1007/s00367-020-00641-z
- Bull, S., Cartwright, J., and Huuse, M. (2009). A Review of Kinematic Indicators from Mass-Transport Complexes Using 3D Seismic Data. *Mar. Pet. Geology*. 26, 1132–1151. doi:10.1016/j.marpetgeo.2008.09.011
- Butler, R. W. H., Eggenhuisen, J. T., Houghton, P., and McCaffrey, W. D. (2016). Interpreting Syndepositional Sediment Remobilization and Deformation beneath Submarine Gravity Flows; a Kinematic Boundary Layer Approach. *J. Geol. Soc.* 173, 46–58. doi:10.1144/jgs2014-150
- Butler, R. W. H., and McCaffrey, W. D. (2010). Structural Evolution and Sediment Entrainment in Mass-Transport Complexes: Outcrop Studies from Italy. *J. Geol. Soc.* 167, 617–631. doi:10.1144/0016-76492009-041
- Cristallini, E., Bottesi, G., Gavarrino, A., Rodriguez, L., Tomezzoli, R., and Cameron, R. (2006). Synrift Geometry of the Neuquén Basin in Northeastern Neuquén Province, Argentina. *Spec. Pap. Geol. Soc. Am.* 407, 147–161. doi:10.1130/SPE407
- Cumberpatch, Z. A., Soutter, E. L., Kane, I. A., Casson, M., and Vincent, S. J. (2021). Evolution of a Mixed Siliciclastic-carbonate Deep-marine System on an Unstable Margin: The Cretaceous of the Eastern Greater Caucasus, Azerbaijan. *Basin Res.* 33, 612–647. doi:10.1111/bre.12488
- Dakin, N., Pickering, K. T., Mohrig, D., and Bayliss, N. J. (2013). Channel-like Features Created by Erosive Submarine Debris Flows: Field Evidence from the Middle Eocene Ainsa Basin, Spanish Pyrenees. *Mar. Pet. Geology*. 41, 62–71. doi:10.1016/j.marpetgeo.2012.07.007
- Damborenea, S. E. (1990). Middle Jurassic Inoceramids from Argentina. *J. Paleontol.* 64, 736–759. doi:10.1017/s0022336000018965
- Davis, C., Houghton, P., McCaffrey, W., Scott, E., Hogg, N., and Kitching, D. (2009). Character and Distribution of Hybrid Sediment Gravity Flow Deposits

- from the Outer Forties Fan, Palaeocene Central North Sea, UKCS. *Mar. Pet. Geol.* 26, 1919–1939. doi:10.1016/j.marpetgeo.2009.02.015
- De La Cruz, R., and Suarez, M. (1997). El Jurásico de la cuenca de Neuquén en lonquimay, Chile: formación nacientes del biobío (38–39°S). *Rev. Geol. Chile* 24, 3–24.
- Dykstra, M. (2005). “Dynamics of Submarine Sediment Mass-Transport, from the Shelf to the Deep Sea.” PhD Thesis Santa Barbara: University of California, Santa Barbara.
- Dykstra, M., Garyfalou, K., Kertzus, V., Kneller, B. C., Milana, J. P., Molinaro, M., et al. (2011). in *Mass-transport Deposits: Combining Outcrop Studies and Seismic Forward Modeling to Understand Lithofacies Distributions, Deformation, and Their Seismic Expression*. Editors H. Posamentier, P. Weimer, and C. Ship (Denver: SEPM Special Publication), 95, 295–310.
- Eggenhuisen, J. T., McCaffrey, W. D., Haughton, P. D. W., and Butler, R. W. H. (2011). Shallow Erosion beneath Turbidity Currents and its Impact on the Architectural Development of Turbidite Sheet Systems. *Sedimentology* 58, 936–959. doi:10.1111/j.1365-3091.2010.01190.x
- Fairweather, L. (2014). “Mechanisms of Supra MTD Topography Generation and the Interaction of Turbidity Currents with Such Deposits,” 242. PhD Thesis University of Aberdeen.
- Fallgatter, C., Kneller, B., Paim, P. S. G., and Milana, J. P. (2017). Transformation, Partitioning and Flow-deposit Interactions during the Run-Out of Megafloes. *Sedimentology* 64, 359–387. doi:10.1111/sed.12307
- Festa, A., Ogata, K., Pini, G. A., Dilek, Y., and Alonso, J. L. (2016). Origin and Significance of Olistostromes in the Evolution of Orogenic Belts: A Global Synthesis. *Gondwana Res.* 39, 180–203. doi:10.1016/j.gr.2016.08.002
- Flores, G. (1955). “Les résultats des études pour les recherches pétrolifères en Sicile: Discussion,” in Proceedings of the 4th World Petroleum Congress 1955 (Rome: Carlo Colombo), 121–122.
- Franzese, J. R., and Spalletti, L. A. (2001). Late Triassic-Early Jurassic continental Extension in Southwestern Gondwana: Tectonic Segmentation and Pre-break-up Rifting. *J. South Am. Earth Sci.* 14, 257–270. doi:10.1016/s0895-9811(01)00029-3
- Franzese, J., Spalletti, L., Pérez, I. G., and Macdonald, D. (2003). Tectonic and Paleoenvironmental Evolution of Mesozoic Sedimentary Basins along the Andean Foothills of Argentina (32°–54°S). *J. South Am. Earth Sci.* 16, 81–90. doi:10.1016/s0895-9811(03)00020-8
- Frey Martinez, J., Cartwright, J., and Hall, B. (2005). 3D Seismic Interpretation of Slump Complexes: Examples from the continental Margin of Israel. *Basin Res.* 17, 83–108. doi:10.1111/j.1365-2117.2005.00255.x
- Fugelli, E. M. G., and Olsen, T. R. (2007). Delineating Confined Slope Turbidite Systems Offshore mid-Norway: The Cretaceous Deep-marine Lysing Formation. *Bulletin* 91, 1577–1601. doi:10.1306/07090706137
- Gee, M. J. R., Gawthorpe, R. L., and Friedmann, S. J. (2006). Triggering and Evolution of a Giant Submarine Landslide, Offshore Angola, Revealed by 3D Seismic Stratigraphy and Geomorphology. *J. Sediment. Res.* 76, 9–19. doi:10.2110/jsr.2006.02
- Gulisano, C. A., Gutiérrez Pleimling, A. R., and Digregorio, J. H. (1984). Esquema estratigráfico de la secuencia jurásica del oeste de la provincia del Neuquén. IX Congr. *Geológico Argentino* 1, 236–259.
- Gulisano, C., and Gutiérrez Pleimling, A. R. (1995). Field Guide. The Jurassic of the Neuquén Basin. a) Neuquén Province: Asociación Geológica Argentina. *Serie E* 2, 1–111.
- Hampton, M. A., Lee, H. J., and Locat, J. (1995). Submarine Landslides. *Rev. Geophys.* 34, 33–59.
- Hansen, L. A. S., Hodgson, D. M., Pontén, A., Bell, D., and Flint, S. (2019). Quantification of basin-floor Fan Pinchouts: Examples from the Karoo Basin, South Africa. *Front. Earth Sci.* 7, 1–20. doi:10.3389/feart.2019.00012
- Hansen, L. A. S., Hodgson, D. M., Pontén, A., Thrana, C., and Obradors Latre, A. (2021). Mixed Axial and Transverse Deep-Water Systems: The Cretaceous post-rift Lysing Formation, Offshore Norway. *Basin Res.* 33, 2229–2251. doi:10.1111/bre.12555
- Haughton, P., Davis, C., McCaffrey, W., and Barker, S. (2009). Hybrid Sediment Gravity Flow Deposits - Classification, Origin and Significance. *Mar. Pet. Geology* 26, 1900–1918. doi:10.1016/j.marpetgeo.2009.02.012
- Haughton, P. D. W., Barker, S. P., and McCaffrey, W. D. (2003). ‘Linked’ Debrisites in Sand-Rich Turbidite Systems - Origin and Significance. *Sedimentology* 50, 459–482. doi:10.1046/j.1365-3091.2003.00560.x
- Hodgson, D. M. (2009). Distribution and Origin of Hybrid Beds in Sand-Rich Submarine Fans of the Tanqua Depocentre, Karoo Basin, South Africa. *Mar. Pet. Geol.* 26, 1940–1956. doi:10.1016/j.marpetgeo.2009.02.011
- Hodgson, D. M., Brooks, H. L., Ortiz-Karpf, A., Spychala, Y., Lee, D. R., and Jackson, C. A.-L. (2019). Entrainment and Abrasion of Megaclasts during Submarine Landsliding and Their Impact on Flow Behaviour. *Geol. Soc. Lond. Spec. Publications* 477, 223–240. doi:10.1144/sp477.26
- Howell, J. A., Schwarz, E., Spalletti, L. A., and Veiga, G. D. (2005). The Neuquén Basin: an Overview. *Geol. Soc. Lond. Spec. Publications* 252, 1–14. doi:10.1144/gsl.sp.2005.252.01.01
- Iverson, R. M. (1997). The Physics of Debris Flows. *Rev. Geophys.* 35, 245–296. doi:10.1029/97rg00426
- Jackson, C. A.-L., and Johnson, H. D. (2009). Sustained Turbidity Currents and Their Interaction with Debrite-Related Topography; Labuan Island, Offshore NW Borneo, Malaysia. *Sediment. Geology* 219, 77–96. doi:10.1016/j.sedgeo.2009.04.008
- Jackson, C. A.-L. (2011). Three-dimensional Seismic Analysis of Megaclast Deformation within a Mass Transport deposit; Implications for Debris Flow Kinematics. *Geology* 39, 203–206. doi:10.1130/g31767.1
- Jobe, Z. R., Lowe, D. R., and Morris, W. R. (2012). *Climbing-ripple Successions in Turbidite Systems: Depositional Environments, Sedimentation Rates and Accumulation Times*, 59, 867–898. doi:10.1111/j.1365-3091.2011.01283.x
- Kamo, S. L., and Riccardi, A. C. (2009). A New U-Pb Zircon Age for an Ash Layer at the Bathonian-Callovia Boundary, Argentina. *Gff* 131, 177–182. doi:10.1080/11035890902867605
- Kane, I. A., and Pontén, A. S. M. (2012). Submarine Transitional Flow Deposits in the Paleogene Gulf of Mexico. *Geology* 40, 1119–1122. doi:10.1130/g33410.1
- Kane, I. A., Pontén, A. S. M., Vangdal, B., Eggenhuisen, J. T., Hodgson, D. M., and Spychala, Y. T. (2017). The Stratigraphic Record and Processes of Turbidity Current Transformation across Deep-marine Lobes. *Sedimentology* 64, 1236–1273. doi:10.1111/sed.12346
- Kleverlaan, K. (1987). Gordo Megabed: a Possible Seismitite in a Tortonian Submarine Fan, Tabernas basin, Province Almería, Southeast Spain. *Sediment. Geology* 51, 165–180. doi:10.1016/0037-0738(87)90047-9
- Kneller, B. C., and Branney, M. J. (1995). Sustained High-Density Turbidity Currents and the Deposition of Thick Massive Sands. *Sedimentology* 42, 607–616. doi:10.1111/j.1365-3091.1995.tb00395.x
- Kneller, B., Dykstra, M., Fairweather, L., and Milana, J. P. (2016). Mass-transport and Slope Accommodation: Implications for Turbidite sandstone Reservoirs. *Bulletin* 100, 213–235. doi:10.1306/09011514210
- Könitzer, S. F., Davies, S. J., Stephenson, M. H., and Leng, M. J. (2014). Depositional Controls on Mudstone Lithofacies in a Basinal Setting: Implications for the Delivery of Sedimentary Organic Matter. *J. Sediment. Res.* 84, 198–214. doi:10.2110/jsr.2014.18
- Lababe, P., Mutti, E., and Seguret, M. (1987). Megaturbidites: A Depositional Model from the Eocene of the SW-Pyrenean Foreland basin, Spain. *Geo-Marine Lett.* 7, 91–101. doi:10.1007/bf02237988
- Leanza, H. A., Mazzini, A., Corfu, F., Llambías, E. J., Svensen, H., Planke, S., et al. (2013). The Chachil Limestone (Pliensbachian-Earliest Toarcian) Neuquén Basin, Argentina: U-Pb Age Calibration and its Significance on the Early Jurassic Evolution of Southwestern Gondwana. *J. South Am. Earth Sci.* 42, 171–185. doi:10.1016/j.jsames.2012.07.012
- Lee, C., Nott, J. A., Keller, F. B., and Parrish, A. R. (2004). Seismic Expression of the Cenozoic Mass Transport Complexes deepwater Tarfaya-Agadir Basin Offshore Morocco. *Proc. Annu. Offshore Technol. Conf.* 3, 1891–1908. doi:10.4043/16741-ms
- Legarreta, L. (1991). Evolution of a Callovian-Oxfordian Carbonate Margin in the Neuquén Basin of West-central Argentina: Facies, Architecture, Depositional Sequences and Global Sea-Level Changes. *Sediment. Geol.* 70 (2-4), 209–240. doi:10.1016/0037-0738(91)90142-Z
- Legarreta, L., and Gulisano, C. A. (1989). “Análisis estratigráfico secuencial de la Cuenca Neuquina (Triásico superior-Terciario inferior),” in *Cuencas Sedimentarias Argentinas*, 221–243.
- Legarreta, L., and Uliana, M. A. (1996). The Jurassic Succession in West-central Argentina: Stratal Patterns, Sequences and Paleogeographic Evolution. *Palaeoogeogr. Palaeoecol.* 120, 303–330. doi:10.1016/0031-0182(95)00042-9

- Legros, F. (2002). Can Dispersive Pressure Cause Inverse Grading in Grain Flows? *J. Sediment. Res.* 72, 166–170. doi:10.1306/041301720166
- Lien, T. (2005). From Rifting to Drifting: Effects on the Development of Deep-Water Hydrocarbon Reservoirs in a Passive Margin Setting, Norwegian Sea. *Norwegian J. Geo.* 85 (4), 319–332.
- Llambias, E. J., Leanza, H. A., and Carbone, O. (2007). Evolución Tectono-magmática durante el pérmico al Jurásico temprano en la Cordillera del Viento (37°05'S - 37°15'S): Nuevas evidencias geológicas y geoquímicas Del Inicio de la Cuenca Neuquina. *Rev. La Asoc. Geol. Argentina* 62, 217–235.
- Llambias, E. J., and Leanza, H. A. (2005). Depósitos laháricos en la formación los molles en chacay melehue, neuquén: Evidencia de volcanismo jurásico en la cuenca neuquina. *Rev. La Asoc. Geol. Argentina* 60, 552–558.
- Llambias, E. J., Quenardelle, S., and Montenegro, T. (2003). The Choiyoi Group from central Argentina: A Subalkaline Transitional Alkaline Association in the Craton Adjacent to the Active Margin of the Gondwana Continent. *J. South. Am. Earth Sci.* 16, 243–257. doi:10.1016/S0895-9811(03)00070-1
- Lowe, D. R. (1982). Sediment Gravity Flows; II, Depositional Models with Special Reference to the Deposits of High-Density Turbidity Currents. *J. Sediment. Res.* 52, 279–297. doi:10.1306/212f7f31-2b24-11d7-8648000102c1865d
- Lowe, D. R., and Guy, M. (2000). Slurry-flow Deposits in the Britannia Formation (Lower Cretaceous), North Sea: A New Perspective on the Turbidity Current and Debris Flow Problem. *Sedimentology* 47, 31–70. doi:10.1046/j.1365-3091.2000.00276.x
- Lucente, C. C., and Pini, G. A. (2003). Anatomy and Emplacement Mechanism of a Large Submarine Slide within a Miocene Foredeep in the Northern Apennines, Italy: A Field Perspective. *Am. J. Sci.* 303, 565–602. doi:10.2475/ajs.303.7.565
- Major, J. J., and Iverson, R. M. (1999). Debris-flow Deposition: Effects of Pore-Fluid Pressure and Friction Concentrated at Flow Margins. *Bull. Geol. Soc. Am.* 111, 1424–1434. doi:10.1130/0016-7606(1999)111<1424:dfdeop>2.3.co;2
- Maceda, R., and Figueroa, D. (1995). Inversion of the Mesozoic Neuquen Rift in the Malargue Fold and Thrust belt, Mendoza, Argentina. *Pet. Basins South. Am.* 62, 369–382.
- McClelland, H. L. O., Woodcock, N. H., and Gladstone, C. (2011). Eye and Sheath Folds in Turbidite Convolute Lamination: Aberystwyth Grits Group, Wales. *J. Struct. Geology* 33, 1140–1147. doi:10.1016/j.jsg.2011.05.007
- McGilvery, T. A., Cook, D. L., and Roberts, H. (2003). “The Influence of Local Gradients on Accommodation Space and Linked Depositional Elements across a Stepped Slope Profile, Offshore Brunei,” in *Shelf margin deltas and linked down slope petroleum systems: Global significance and future exploration potential: Gulf Coast Section SEPM 23rd Annual Research Conference*, 387–419. doi:10.5724/gcs.03.23.0387
- Migeon, S., Ceramicola, S., Praeg, D., Ducassou, E., Dano, A., Ketzner, J. M., et al. (2014). “Post-failure Processes on the Continental Slope of the Central Nile Deep-Sea Fan: Interactions between Fluid Seepage, Sediment Deformation and Sediment-Wave Construction,” in *Submarine Mass Movements and Their Consequences. Advances in Natural and Technological Hazards Research* (Cham: Springer), Vol 37, 117–127. doi:10.1007/978-3-319-00972-8_11
- Moscardelli, L., Wood, L., and Mann, P. (2006). Mass-transport Complexes and Associated Processes in the Offshore Area of Trinidad and Venezuela. *Bulletin* 90, 1059–1088. doi:10.1306/02210605052
- Moscardelli, L., and Wood, L. (2008). New Classification System for Mass Transport Complexes in Offshore Trinidad. *Basin Res.* 20, 73–98. doi:10.1111/j.1365-2117.2007.00340.x
- Mulder, T., and Alexander, J. (2001). The Physical Character of Subaqueous Sedimentary Density Flows and Their Deposits. *Sedimentology* 48, 269–299. doi:10.1046/j.1365-3091.2001.00360.x
- Mutti, E. (1977). Distinctive Thin-Bedded Turbidite Facies and Related Depositional Environments in the Eocene Hecho Group (South-central Pyrenees, Spain). *Sedimentology* 24, 107–131. doi:10.1111/j.1365-3091.1977.tb00122.x
- Nardin, T. R., Hein, F. J., Gorsline, D. S., and Edwards, B. D. (1979). A Review of Mass Movement Processes, Sediment and Acoustic Characteristics, and Contrasts in Slope and Base-Of-Slope Systems versus Canyon-fan-basin Floor Systems. *SEPM Spec. Publ.* 27, 61–73. doi:10.2110/pec.79.27.0061
- Nwoko, J., Kane, I., and Huuse, M. (2020a). Megaclasts within Mass-Transport Deposits: Their Origin, Characteristics and Effect on Substrates and Succeeding Flows. *Geol. Soc. Lond. Spec. Publications* 500, 515–530. doi:10.1144/sp500-2019-146
- Nwoko, J., Kane, I., and Huuse, M. (2020b). Mass Transport deposit (MTD) Relief as a Control on post-MTD Sedimentation: Insights from the Taranaki Basin, Offshore New Zealand. *Mar. Pet. Geology* 120, 104489. doi:10.1016/j.marpetgeo.2020.104489
- Ogata, K., Festa, A., Pini, G. A., and Alonso, J. L. (2019). “Submarine Landslide Deposits in Orogenic Belts: Olistostromes and Sedimentary Mélanges,” in *Submarine Landslides: Subaqueous Mass Transport Deposits from Outcrops to Seismic Profiles* (American Geophysical Union), 1–26.
- Ogata, K., Mountjoy, J. J., Pini, G. A., Festa, A., and Tinterri, R. (2014a). Shear Zone Liquefaction in Mass Transport deposit Emplacement: A Multi-Scale Integration of Seismic Reflection and Outcrop Data. *Mar. Geology* 356, 50–64. doi:10.1016/j.margeo.2014.05.001
- Ogata, K., Mutti, E., Pini, G. A., and Tinterri, R. (2012). Mass Transport-Related Stratal Disruption within Sedimentary Mélanges: Examples from the Northern Apennines (Italy) and South-central Pyrenees (Spain). *Tectonophysics* 568–569, 185–199. doi:10.1016/j.tecto.2011.08.021
- Ogata, K., Pogačnik, Ž., Pini, G. A., Tunis, G., Festa, A., Camerlenghi, A., et al. (2014b). The Carbonate Mass Transport Deposits of the Paleogene Friuli Basin (Italy/Slovenia): Internal Anatomy and Inferred Genetic Processes. *Mar. Geology* 356, 88–110. doi:10.1016/j.margeo.2014.06.014
- Ortiz-Karpf, A., Hodgson, D. M., Jackson, C. A.-L., and McCaffrey, W. D. (2017). Influence of Seabed Morphology and Substrate Composition on Mass-Transport Flow Processes and Pathways: Insights from the Magdalena Fan, Offshore Colombia. *J. Sediment. Res.* 87, 189–209. doi:10.2110/jsr.2017.10
- Ortiz-Karpf, A., Hodgson, D. M., and McCaffrey, W. D. (2015). The Role of Mass-Transport Complexes in Controlling Channel Avulsion and the Subsequent Sediment Dispersal Patterns on an Active Margin: The Magdalena Fan, Offshore Colombia. *Mar. Pet. Geology* 64, 58–75. doi:10.1016/j.marpetgeo.2015.01.005
- Owen, G. (1987). Deformation Processes in Unconsolidated Sands. *Geol. Soc. Lond. Spec. Publications* 29, 11–24. doi:10.1144/gsl.sp.1987.029.01.02
- Owen, G. (2003). Load Structures: Gravity-Driven Sediment Mobilization in the Shallow Subsurface. *Geol. Soc. Lond. Spec. Publications* 216, 21–34. doi:10.1144/gsl.sp.2003.216.01.03
- Pángaro, F., Pereira, D. M., and Micucci, E. (2009). El sinrift de la dorsal de Huinac, Cuenca Neuquina: Evolución y control sobre la estratigrafía y estructura del área. *Rev. La Asoc. Geol. Argentina* 65, 265–277.
- Payros, A., and Pujalte, V. (2019). “Eocene Mass-Transport Deposits in the Basque Basin (Western Pyrenees, Spain) Insights Into Mass-Flow Transformation and Bulldozing Processes,” in *Submarine Landslides: Subaqueous Mass Transport Deposits from Outcrops to Seismic Profiles*. Editors K. Ogata, A. Festa, and A. G. Pini (American Geophysical Union), 155–170. doi:10.1002/9781119500513.ch10
- Payros, A., Pujalte, V., and Orue-Etxebarria, X. (1999). The South Pyrenean Eocene Carbonate Megabreccias Revisited: New Interpretation Based on Evidence from the Pamplona Basin. *Sediment. Geology* 125, 165–194. doi:10.1016/s0037-0738(99)00004-4
- Pickering, K. T., and Corregidor, J. (2005). Mass-transport Complexes (MTCs) and Tectonic Control on basin-floor Submarine Fans, Middle Eocene, South Spanish Pyrenees. *J. Sediment. Res.* 75, 761–783. doi:10.2110/jsr.2005.062
- Prélat, A., Hodgson, D. M., and Flint, S. S. (2009). Evolution, Architecture and Hierarchy of Distributary Deep-Water Deposits: a High-Resolution Outcrop Investigation from the Permian Karoo Basin, South Africa. *Sedimentology* 56, 2132–2154. doi:10.1111/j.1365-3091.2009.01073
- Privat, A. M. J., Hodgson, D. M., Jackson, C. A., Schwarz, E., and Peakall, J. (2021). Evolution from Syn-rift Carbonates to Early post-rift Deep-marine Intraslope Lobes: The Role of Rift basin Physiography on Sedimentation Patterns. *Sedimentology* 68, 2563–2605. doi:10.1111/sed.12864
- Riccardi, A. C., Damborenea, S. E., Manceño, M. O., and Leanza, H. A. (2011). *Megainvertebrados del Jurásico y su importancia geobiológica. Relat. del XVIII Congr. Neuquén: Geológico Argentino*, 441–464.
- Riccardi, A. C. (2008). The marine Jurassic of Argentina: A Biostratigraphic Framework. *Episodes* 31, 326–335. doi:10.18814/epiugs/2008/v31i3/007
- Riccardi, A., and Kamo, S. (2014). “Biostratigraphy and Geochronology of the Pliensbachian-Toarcan Boundary in Argentina,” in XIX Congr. Geológico Argentino, Córdoba, Argentina, Junio 2014, 9–11.
- Rosenfeld, U., and Vollstaedter, W. (1980). *Turbidite und andere Rhythmite im tieferen Jura des Neuquén-Beckens* Argentinien: Pascal and Francis Bibliographic Databases, 379–421.

- Sawyer, D. E., Flemings, P. B., Dugan, B., and Germaine, J. T. (2009). Retrogressive Failures Recorded in Mass Transport Deposits in the Ursa Basin, Northern Gulf of Mexico. *J. Geophys. Res. Solid Earth* 114, 1–20. doi:10.1029/2008jb006159
- Sinclair, H. D., and Tomasso, M. (2002). Depositional Evolution of Confined Turbidite Basins. *J. Sediment. Res.* 72, 451–456. doi:10.1306/111501720451
- Sobiesiak, M. S., Kneller, B., Alsop, G. I., and Milana, J. P. (2016). Internal Deformation and Kinematic Indicators within a Tripartite Mass Transport deposit, NW Argentina. *Sediment. Geology*. 344, 364–381. doi:10.1016/j.sedgeo.2016.04.006
- Southern, S. J., Patacci, M., Felletti, F., and McCaffrey, W. D. (2015). Influence of Flow Containment and Substrate Entrapment upon sandy Hybrid Event Beds Containing a Co-genetic Mud-Clast-Rich Division. *Sediment. Geology*. 321, 105–122. doi:10.1016/j.sedgeo.2015.03.006
- Soutter, E. L., Kane, I. A., Fuhrmann, A., Cumberpatch, Z. A., and Huuse, M. (2019). The Stratigraphic Evolution of Onlap in Siliciclastic Deep-Water Systems: Autogenic Modulation of Allogenic Signals. *J. Sediment. Res.* 89, 890–917. doi:10.2110/jsr.2019.49
- Soutter, E. L., Kane, I. A., and Huuse, M. (2018). Giant Submarine Landslide Triggered by Paleocene Mantle Plume Activity in the North Atlantic. *Geology* 46, 511–514. doi:10.1130/g40308.1
- Spalletti, L. A., Parent, H., Veiga, G. D., and Schwarz, E. (2012). Amonites y bioestratigrafía del Grupo Cuyo en la Sierra de Reyes (cuenca Neuquina central, Argentina) y su significado secuencial. *Andean Geol.* 39, 464–481. doi:10.5027/andgeov39n3-a06
- Spychala, Y. T., Hodgson, D. M., Prélat, A., Kane, I. A., Flint, S. S., and Mountney, N. P. (2017a). Frontal and Lateral Submarine Lobe Fringes: Comparing Sedimentary Facies, Architecture and Flow Processes. *J. Sediment. Res.* 87, 75–96. doi:10.2110/jsr.2017.2
- Spychala, Y. T., Hodgson, D. M., Stevenson, C. J., and Flint, S. S. (2017b). Aggradational Lobe Fringes: The Influence of Subtle Intra-basinal Seabed Topography on Sediment Gravity Flow Processes and Lobe Stacking Patterns. *Sedimentology* 64, 582–608. doi:10.1111/sed.12315
- Stevenson, C. J., Jackson, C. A., Hodgson, D. M., Hubbard, S. M., and Eggenhuisen, J. T. (2015). Deep-water Sediment Bypass. *J. Sediment. Res.* 85 (9), 1058–1081. doi:10.2110/jsr.2015.63
- Stevenson, C. J., Peakall, J., Hodgson, D. M., Bell, D., and Privat, A. (2020). TB or Not TB: Banding in Turbidite Sandstones. *J. Sediment. Res.* 90, 821–842. doi:10.2110/jsr.2020.43
- Stevenson, M. J., Jackson, C. A., Johnson, H. D., and Hodgson, D. M. (2021). Evolution of a Sand-Rich Submarine Channel–Lobe System, and the Impact of Mass-Transport and Transitional-Flow Deposits on Reservoir Heterogeneity: Magnus Field, Northern North Sea. *Petroleum Geosci.* 27.
- Stevenson, M. J., Jackson, C. A.-L., Hodgson, D. M., and Johnson, H. D. (2020). Lateral Variability of Shelf-Edge and basin-floor Deposits, Santos Basin, Offshore Brazil. *J. Sediment. Res.* 90, 1198–1221. doi:10.2110/jsr.2020.14
- Stow, D. A. V., and Johansson, M. (2000). Deep-water Massive Sands: Nature, Origin and Hydrocarbon Implications. *Mar. Pet. Geology*. 17, 145–174. doi:10.1016/s0264-8172(99)00051-3
- Suárez, M., and De la Cruz, R. (1997). “Volcanismo pliniano del Lías durante los inicios de la cuenca de Neuquén, Cordillera del Viento, Neuquén, Argentina,” in *Congreso Geológico Chileno*, 266–270.
- Sumner, E. J., Amy, L. A., and Talling, P. J. (2008). Deposit Structure and Processes of Sand Deposition from Decelerating Sediment Suspensions. *J. Sediment. Res.* 78, 529–547. doi:10.2110/jsr.2008.062
- Talling, P. J., Amy, L. A., and Wynn, R. B. (2007). New Insight into the Evolution of Large-Volume Turbidity Currents: Comparison of Turbidite Shape and Previous Modelling Results. *Sedimentology* 54, 737–769. doi:10.1111/j.1365-3091.2007.00858.x
- Talling, P. J., Masson, D. G., Sumner, E. J., and Malgesini, G. (2012). Subaqueous Sediment Density Flows: Depositional Processes and deposit Types. *Sedimentology* 59, 1937–2003. doi:10.1111/j.1365-3091.2012.01353.x
- Tinterri, R. (2011). Combined Flow Sedimentary Structures and the Genetic Link between Sigmoidal-And Hummocky-Cross Stratification. *GeoActa* 10 (4), 1–43.
- Tinterri, R., Muzzi Magalhaes, P., Tagliaferri, A., and Cunha, R. S. (2016). Convolute Laminations and Load Structures in Turbidites as Indicators of Flow Reflections and Decelerations against Bounding Slopes. Examples from the Marnoso-Arenacea Formation (Northern Italy) and Annot Sandstones (South Eastern France). *Sediment. Geology*. 344, 382–407. doi:10.1016/j.sedgeo.2016.01.023
- Trabucho-Alexandre, J., Dirkx, R., Veld, H., Klaver, G., and De Boer, P. L. (2012). Toarcian Black Shales in the Dutch central Graben: Record of Energetic, Variable Depositional Conditions during an Oceanic Anoxic Event. *J. Sediment. Res.* 82, 104–120. doi:10.2110/jsr.2012.5
- Twiss, R. J., and Moores, E. M. (1992). *Structural Geology*. New York: W.H. Freeman and Company.
- Valdez, V., Milana, J. P., Sobiesiak, M. S., and Kneller, B. (2019). “The Carboniferous MTD Complex at La Peña Canyon, Paganzo Basin (San Juan, Argentina),” in *Submarine Landslides: Subaqueous Mass Transport Deposits from Outcrops to Seismic Profiles* (American Geophysical Union), p. 105–116.
- Van Der Merwe, W. C., Hodgson, D. M., and Flint, S. S. (2011). Origin and Terminal Architecture of a Submarine Slide: A Case Study from the Permian Vischkuil Formation, Karoo Basin, South Africa. *Sedimentology* 58, 2012–2038. doi:10.1111/j.1365-3091.2011.01249.x
- Van der Merwe, W. C., Hodgson, D. M., and Flint, S. S. (2009). Widespread Syn-Sedimentary Deformation on a Muddy Deep-Water basin-floor: The Vischkuil Formation (Permian), Karoo Basin, South Africa. *Basin Res.* 21, 389–406. doi:10.1111/j.1365-2117.2009.00396.x
- Veiga, G. D., Schwarz, E., and Spalletti, L. A. (2011). Análisis estratigráfico de la Formación Lotena (Calloviano superior- Oxfordiano inferior) en la Cuenca Neuquina Central, República Argentina. Integración de información de afloramientos y subsuelo. *Andean Geol.* 38, 171–197. doi:10.5027/andgeov38n1-a10
- Veiga, G. D., Schwarz, E., Spalletti, L. A., and Massafiero, J. L. (2013). Anatomy and Sequence Architecture of the Early Post-Rift in the Neuquen Basin (Argentina): A Response to Physiography and Relative Sea-Level Changes. *J. Sediment. Res.* 83, 746–765. doi:10.2110/jsr.2013.56
- Vergani, G. D., Tankard, A. J., Belotti, H. J., and Welsink, H. J. (1995/1904). *Tectonic Evolution and Paleogeography of the Neuquén Basin*. Argentina: Pet. basins South Am., 383–402.
- Vicente, J. C. (2005). Dynamic Paleogeography of the Jurassic Andean Basin: Pattern of Transgression and Localisation of Main Straits through the Magmatic Arc. *Rev. La Asoc. Geol. Argentina* 60, 221–250.
- Watt, S. F. L., Talling, P. J., Vardy, M. E., Masson, D. G., Henstock, T. J., Hühnerbach, V., et al. (2012). Widespread and Progressive Seafloor-Sediment Failure Following Volcanic Debris Avalanche Emplacement: Landslide Dynamics and Timing Offshore Montserrat, Lesser Antilles. *Mar. Geology*. 323–325, 69–94. doi:10.1016/j.margeo.2012.08.002
- Weaver, C. (1942). “A General Summary of the Mesozoic of South and Central America,” in Proceedings of the eighth American scientific congress held, Washington, May 10–18, 149–193.
- Weaver, C. (1931). *Paleontology of the Jurassic and Cretaceous of West Central Argentina*, 1. Seattle: Memoir University of Washington.
- Zöllner, W., and Amos, A. J. (1973). *Descripción geológica de la hoja 32b*. Chos Malal: Servicio Geológico Nacional, 97.

Conflict of Interest: The authors declare that the research was conducted in the absence of any commercial or financial relationships that could be construed as a potential conflict of interest.

Publisher’s Note: All claims expressed in this article are solely those of the authors and do not necessarily represent those of their affiliated organizations, or those of the publisher, the editors and the reviewers. Any product that may be evaluated in this article, or claim that may be made by its manufacturer, is not guaranteed or endorsed by the publisher.

Copyright © 2021 Martínez-Doñate, Privat, Hodgson, Jackson, Kane, Spychala, Duller, Stevenson, Keavney, Schwarz and Flint. This is an open-access article distributed under the terms of the Creative Commons Attribution License (CC BY). The use, distribution or reproduction in other forums is permitted, provided the original author(s) and the copyright owner(s) are credited and that the original publication in this journal is cited, in accordance with accepted academic practice. No use, distribution or reproduction is permitted which does not comply with these terms.